Comparing high-latitude thermospheric winds from FPI and CHAMP accelerometer measurements

Anasuya Aruliah[1,] Matthias Förster[2,3], Rosie Hood[1], Ian McWhirter[1], Eelco Doornbos[4,5]

[1]Atmospheric Physics Laboratory, University College London, Gower Street, London, WC1E 6BT, UK
[2]Helmholtz-Zentrum Potsdam, GFZ German Research Centre for Geosciences, Telegrafenberg, 14473 Potsdam, Germany
[3]Max Planck Institute for Solar System Research (MPS), Justus-von-Liebig-Weg 3, 37077 Göttingen, Germany
[4]Old affiliation: Faculty of Aerospace Engineering, Delft University of Technology (TU Delft), Kluyverweg 1, 2629 HS Delft, The Netherlands
[5]Current affiliation: Royal Netherlands Meteorological Institute (KNMI), Utrechtseweg 297, 3731 GA De Bilt, The Netherlands

Correspondence to: Anasuya Aruliah (a.aruliah@ucl.ac.uk), Matthias Förster (mfo@gfz-potsdam.de) and Eelco Doornbos (eelco.doornbos@knmi.nl)

Abstract. It is generally assumed that horizontal wind velocities are independent of height above the F_1-region (> 300 km) due to the large molecular viscosity of the upper thermosphere. This assumption is used to compare two completely different methods of thermospheric neutral wind observation, using two distinct locations in the high-latitude Northern Hemisphere. The measurements are from ground-based Fabry-Perot Interferometers (FPI), and from in-situ accelerometer measurements onboard the CHAMP satellite, which was in a near polar orbit. The UCL KEOPS FPI is located in the vicinity of the auroral oval at the ESRANGE site near Kiruna, Sweden (67.8°N, 20.4°E). The UCL Longyearbyen FPI is a polar cap site, located at the Kjell Henriksen Observatory on Svalbard (78.1°N, 16.0°E). The comparison is done in a statistical sense, comparing a longer time series obtained during nighttime hours in the winter months (DOY 300-65); with overflights of the CHAMP satellite between 2001 and 2007 over the observational sites, within ±2° latitude (±230 km horizontal range). The FPI is assumed to measure the line-of-sight winds at ~240 km height, i.e. the peak emission height of the atomic oxygen 630.0 nm emission. The cross-track winds are derived from state-of-the-art precision accelerometer measurements at altitudes between ~450 km (in 2001) to ~350 km (in 2007); i.e. 100-200 km above the FPI wind observations. We show that CHAMP winds at high latitudes are typically 1.5-2 times larger than FPI winds. In addition to testing the consistency of the different measurement approaches, the study aims to clarify the effects of viscosity on the height dependence of thermospheric winds.

1 Introduction

Global circulation models (GCM) of the upper atmosphere (80-600 km altitude) appear in two forms: climatologies based on empirical measurements, and theoretical models that calculate atmospheric conditions using the principles of physics and chemistry. These models are important for space weather studies and are also applied in understanding and predicting drag on low-altitude satellites, space debris, and the study of re-entry of near Earth objects. The theoretical and empirical models rely on observations from ground-based instruments

around the world and global observations by satellites to provide constraints and boundary conditions. In particular, models must account for energy from sources external to the upper atmosphere (i.e., direct solar radiation, particle precipitation and heat flow from above; radiative, conductive and convective heating from below; the magnetospheric electrodynamic driver at high-latitudes), which is divided between acceleration of the gas and heating. The empirical evidence for the energy budget can be provided by observations of winds and temperatures.

The use of accelerometers on satellites to measure thermospheric winds had previously been reported quite rarely (Marcos and Forbes, 1985; Forbes et al., 1993). Over the last few years CHAMP and GOCE winds have been reported (e.g. Förster et al., 2008; Doornbos et al., 2010). The advantage of this technique consists in the fairly direct in-situ measurement, with relatively high spatial (temporal) resolution, of the cross-track wind component along the orbital track with only a limited number of special assumptions for the data interpretation. Adding more satellites (e.g., GRACE and GRACE-FO), should allow better full wind vector reconstructions in terms of statistical averages (Förster et al., 2008; Förster et al., 2017) as well as parameterized statistical studies of the upper thermosphere dynamics in the near future. As a result, it makes it imperative that the derived winds are correct because satellites provide global coverage of the upper atmosphere, unlike the small number of ground-based instruments currently in existence. The larger databases and global coverage of the satellites will particularly influence a semi-empirical model such as the Horizontal Wind Model (Drob et al., 2015), which is commonly used as a climatology of winds to provide initial boundary conditions and validation for physics-based global circulation models (GCMs).

In this paper we show that upper thermospheric winds measured by the CHAMP satellites are typically 1.5 to 2 times larger than those measured by ground-based Fabry-Perot Interferometers (FPIs) at an auroral site and polar cap site. It is imperative to know whether this discrepancy is real (i.e. there is a variation of speed with respect to height), or whether we have uncovered a problem of the absolute scaling of wind measurements by comparing FPIs with CHAMP. With incorrect scaling, there arises a problem of distortion of energy budget calculations of the upper atmosphere. A precise estimation of energy supply to the system is hindered essentially, because the partitioning of kinetic and thermal energy channels becomes obscured. The acceleration of the neutral air in 3-D space with respect to the active driver of the plasma motion is important to estimate, for instance, the Joule heating rate as one of the most important thermal energy inputs. This has a knock-on effect on the calculation of the absolute density of the gas, which is an important parameter used in, for example, satellite orbit calculations.

2 The CHAMP accelerometer data

The challenging mini-satellite payload (CHAMP) was managed by the GFZ German Research Centre for Geosciences of the Helmholtz Centre Potsdam. This mission was designed to perform detailed studies of the Earth's gravitational and magnetic field with unprecedented accuracies and space/time resolutions as well as GPS atmosphere and ionosphere profiling. The spacecraft was launched in July 2000 into a circular near-polar

80   orbit with 87.3° inclination at an initial altitude of ~460 km (Reigber et al., 2002). Its orbital altitude gradually

81   decayed to ~400 km in 2003 and ~330 km in 2008, and ended in September 2010.

82

83   One key scientific instrument onboard CHAMP was a triaxial accelerometer. It was located at the spacecraft's

84   center of mass and effectively probed the in-situ air drag. Thermospheric mass density and cross-track neutral

85   wind can be obtained from the drag acceleration observations. It is very difficult to determine the error estimate

86   because it depends on several variables as discussed in Doornbos et al. (2010) and shown in Table 5 from Visser

87   et al. (2019). This indicates that for force-derived winds, the largest sensitivity is to energy accommodation,

88   which is of the order of several tens of ms^{-1}.

89

90   A first analysis of the high-latitude thermospheric wind circulation in dependence on the IMF orientation was

91   performed by Förster et al. (2008) using the preliminary methodology of cross-track wind estimations from

92   accelerometer data as described in Liu et al. (2006). Förster et al. (2011) then presented an overview of the

93   average transpolar thermospheric circulation in terms of the vorticity. Here, they made use of the newly

94   calibrated and re-analysed data set that resulted from an ESA study, initiated for the Swarm satellites mission

95   launched in November 2013 (Helleputte et al., 2009). The CHAMP neutral wind data, based on the cross-track

96   accelerometer measurements, are available via the data repository at the GFZ Potsdam (Förster and Doornbos,

97   2019).

98

99   As pointed out by Doornbos et al. (2010), the along-track wind is not resolvable because it induces a similar

100   signal in the acceleration as the density variation. This wind component is ignored, or the value from an

101   empirical wind model is used, because the along-track wind is a relatively small magnitude in comparison with

102   the satellite speed of 7.6 km s^{-1}. The empirical wind model used is, for example, HWM90 (Hedin et al., 1991) or

103   its latest edition HWM14, as published by Drob et al. (2015). In polar areas the along-track wind velocity can

104   achieve up to 10% of the satellite speed. Consequently, the along-track mass density estimation can have an

105   error of about 20% in the polar latitudes, because the acceleration is proportional to the wind velocity squared

106   (e.g., Doornbos et al., 2010). But it is less easy to estimate the error in the cross-track wind in the polar region

107   due to considerably smaller acceleration signals. There are also systematic contributions from other sources such

108   as gas-surface interactions, surface properties, spacecraft shape, spacecraft attitude and radiation pressure

109   accelerations, which make the satellite aerodynamic coefficients difficult to resolve (see Doornbos et al., 2010,

110   and the error budget in Appendix A of that paper; Mehta et al., 2017 and March et al., 2018). The pre-processed

111   data of the accelerometer were re-sampled to 10-sec averages for the further use in this study. Measurements of

112   10-sec cadence correspond to a spatial separation of 76 km or about 2/3° in latitude between the individual data

113   points.

114

115   **3 The Fabry-Perot Interferometer data**

116   The advantage of using Fabry-Perot Interferometers is that they make direct measurements of thermospheric

117   wind speeds using only a few instrumental or geophysical assumptions. They are also generally reliable

118   instruments that can be left to run for months at a time. The FPIs operated by University College London are

119   located at the Kiruna Esrange Optical Platform System (KEOPS) in northern Sweden; and on the island of

120   Svalbard at the Adventdalen Observatory (before November 2006), from which it was moved to the Kjell
121   Henriksen Observatory (after November 2006). The geographic and geomagnetic coordinates of these two
122   stations are given in Table 1 for Kiruna (KEOPS) and Table 2 for Longyearbyen (Svalbard). The Altitude-
123   Adjusted   Corrected   Geomagnetic   Coordinates   (AACGM)   are   obtained   from
124   http://sdnet.thayer.dartmouth.edu/aacgm/aacgm_calc.php#AACGM (Shepherd, 2014). A date of 15 December
125   2002 was used, for an altitude of 240 km. Owing to the large field-of-view of the FPIs (see later) the locations of
126   the volumes observed by the FPIs in the East and West look directions are also given, and the corresponding
127   MLT.

128

129   **Table 1**

FPI Site	Geographic coordinates	AACGM geomagnetic coordinates for 15 Dec 2002 at 240 km altitude	AACGM magnetic local time (MLT) midnight in UT
Kiruna (KEOPS)	67.87°N, 21.03°E	65.08°N, 103.32°E	1.860 UT
Kiruna (KEOPS) EAST	67.87°N, 26.6°E	64.8°N, 107.8°E	2.16 UT
Kiruna (KEOPS) WEST	67.87°N, 15.5°E	65.4°N, 98.9°E	1.57 UT

130
131   **Table 2**

FPI Site	Geographic coordinates	AACGM geomagnetic coordinates for 15 Dec 2002 at 240 km altitude	AACGM magnetic local time (MLT) midnight in UT
Longyearbyen (KHO after 2006)	78.15°N, 16.04°E	75.38°N, 111.80°E	2.43 UT
Longyearbyen EAST (KHO after 2006)	78.15°N, 33.6°E	74.4°N, 123.6°E	3.21 UT
Longyearbyen WEST (KHO after 2006)	78.15°N, -1.5°E	76.8°N, 100.3°E	1.66 UT
Longyearbyen (Adventdalen before 2006)	78.19°N, 15.92°E	75.43°N, 111.80°E	2.43 UT
Longyearbyen EAST (Adventdalen before 2006)	78.19°N, 33.5°E	74.4°N, 123.6°E	3.21 UT
Longyearbyen WEST (Adventdalen before 2006)	78.19°N, -1.7°E	76.9°N, 100.3°E	1.66 UT

132

A significant limitation of ground based FPIs is that optical measurements of airglow and aurora at thermospheric altitudes are only possible during the night when the sun's zenith angle is greater than 98°. This means that the high latitude FPI observing season runs only in the winter months: from September to April at KEOPS; and October to March at Longyearbyen. The FPIs have been nearly continually observing the 630 nm emission from airglow and aurora every winter night since 1981 and 1986, respectively. Complete 24 hours of observation are possible during November to January at Longyearbyen. Thermospheric winds have been monitored by calculating the Doppler shifts of the 630nm airglow radiation intensities. The FPI instrument has a mirror that rotates to look in several directions (e.g. north, north-east, east, south, west, north-west, zenith and a calibration lamp) to provide line-of-sight wind measurements at a fixed elevation angle. The exposure times can be as low as 10 seconds, up to 120 seconds. A typical complete scan cycle takes ~4 minutes for Kiruna and ~5 mins for Longyearbyen. After 1999, when laser calibrations were made possible, thermospheric temperatures were measured from the thermal broadening of the emission line. More details of operation may be found in Aruliah et al. (2005) and references therein.

The 630nm emission has a peak intensity at an altitude of around 240 km. So measurements of the Doppler shifts and thermal broadening of the emission line are used to determine the winds and neutral temperatures of the upper thermosphere (> 200km altitude). The elevation angle of the mirror is 45° for the Kiruna FPI and 30° for the Longyearbyen FPI. Thus the radius of the field-of-view is 240 km and 416 km, respectively, which represents roughly a 5° and 8° separation in latitude of the north and south viewing volumes at the respective sites. At these high latitudes where the magnetospheric dynamo dominates the plasma flows, ion-neutral coupling can create meso-scale structures in the upper thermosphere on horizontal scale sizes of as little as ~100 km (e.g. Aruliah et al., 2001). So average wind speeds have been determined for each of the 4 cardinal look directions in order that the meso-scale structure is not lost. The winds are strongly dependent on UT, season, solar cycle and geomagnetic activity due to the dominant forcing mechanisms of pressure gradients and ion-neutral coupling in the high latitude upper thermosphere. The maximum average wind vector magnitudes measured by an FPI at Kiruna were shown to be in the range 100-300 ms^{-1} and the errors of measurements were around 10-20 ms^{-1} (Aruliah et al., 1996). The main sources of error are:

a) poor signal to noise when the 630 nm intensities are low, such as at solar minimum, or geomagnetically quiet conditions.

b) the existence of large vertical winds. These break the assumption that the winds are predominantly horizontal. Vertical winds are generally small, but can be a few 10s of ms^{-1} at high latitudes (Aruliah and Rees, 1995; Ronksley, 2016). Large vertical winds introduce an error of a few per cent into the calculation of a horizontal wind component from the line-of-sight measurement.

c) the assumption that the neutral winds are nearly constant with respect to altitude above 200 km owing to the very low density and consequently high molecular viscosity of the upper thermosphere.

4 CMAT2 model winds

The UCL Coupled Middle Atmosphere Thermosphere (CMAT2) model is a 3-dimensional, time-dependent physics-based model, that solves numerically the non-linear coupled continuity equations of mass, momentum

170 and energy (Harris et al., 2002). The model has a latitude resolution of 2°, longitude 18°, and a one third scale

171 height for a height range of ~15 km (top of the troposphere) to 300-600km (top of the thermosphere).

172 Thermospheric heating, photodissociation and photoionisation are calculated for solar X-ray, EUV and UV

173 radiation between 0.1-194 nm (Fuller-Rowell, 1992; Torr et al, 1980a and 1980b; Roble, 1987). High latitude

174 ionospheric parameters of ion and electron densities and temperatures, plus field-aligned plasma velocities, are

175 from the Coupled Sheffield University High-latitude Ionosphere Model (Quegan et al., 1982; Fuller-Rowell et

176 al., 1996). The high latitude auroral precipitation is provided by the TIROS/NOAA auroral precipitation model

177 (Fuller-Rowell and Evans, 1987) and the high latitude electric field model is from Foster et al., (1986). Other

178 features are detailed in Harris et al. (2002). The CMAT2 winds will be presented as part of the discussion

179 below.

180

181 **5. Results**

182 Data were chosen from the 3-year periods 2001-2003 and 2005-2007, when the CHAMP satellite was in orbit.

183 These represent periods of solar maximum and minimum, respectively. CHAMP data were collected all year

184 around, but the FPI data were limited to nighttime periods only.

185 **5.1 CHAMP average winds**

186 Figures 1 and 2 show plots of average CHAMP accelerometer measurements of the cross-track thermospheric

187 wind component during the whole period of years 2001–2003, that were obtained during direct overflights

188 above the FPI stations at Longyearbyen (Figure 1) and KEOPS (Figure 2). The cross-track wind component is

189 defined as pointing into the positive y-direction of the S/C coordinate system with its x axis along the orbital

190 trace, the z axis toward nadir, and the y-axis completing the right-hand system. The y-wind component therefore

191 points perpendicular to the orbital plane to the right side, when looking in the direction of flight. Given the high

192 inclination (87.3°) of the CHAMP satellite, this corresponds approximately to the geographically eastward

193 direction for the ascending orbital track (blue lines in Figure 1) except for very high geographic latitudes (see

194 below). The cross-track wind measurements of the descending orbital tracks (red lines) have been flipped in sign

195 to get nearly the same eastward wind component.

196

197 Figure 1a and 2a show average values for all data, while Figures 1b, 1c, 2b and 2c show the summer and winter

198 averages. There are many more data points for the Longyearbyen station, at a higher geographic latitude

199 compared with KEOPS. This confirms the fact that the relative probability of overhead crossings of high-

200 latitude stations by low Earth orbiting (LEO) satellites with a near-polar circular orbit augments with increasing

201 latitude. A statistical study has to make some compromise with respect to the area of accepted local

202 coincidences of the satellite recordings above the ground-based observations and also with regard to the further

203 data binning. Here, a circular area based on a 2° latitude radius and hourly bins versus local time have been used

204 which produces a sufficiently good coverage. Further binnings have been been tested to investigate the effect on

205 the results. A shorter radius deteriorates the statistics within the bin, while larger bins tend to smear the spatial

206 and temporal variations. Data filtering with respect to other parameters like, e.g., season, solar wind and

207 interplanetary magnetic field (IMF) values, solar radiation and geomagnetic activity indices should be taken into
208 account if they appear to make a significant effect.
209
210 The variance of the cross-track neutral wind magnitude is considerably larger during the whole day above the
211 station at higher latitudes. The average phase of the diurnal eastward wind variation differs also considerably
212 between the data sets of the two observatories. The eastward wind maximizes during the pre-midnight hours
213 over Longyearbyen, while a smaller maximum and a shorter interval of eastward wind is seen at lower latitudes
214 above the KEOPS station (2–3 hours versus about 6 hours). The eastward neutral thermospheric wind is
215 approximately sinusoidal for Longyearbyen (Fig. 1a), but reveals two maxima/minima over the KEOPS station
216 (Fig. 2a). The westward wind maximizes there at about 19 LT and prior to midday (~11 LT). Finally, the
217 variance of the cross-track neutral wind magnitude over the lower latitude station KEOPS is relatively large
218 during the afternoon to early nighttime hours (~15–20 LT). This might be due to the position of this station
219 relative to the large dusk cell which is known to be strongly dependent on, in particular, the IMF By component
220 (cf., e.g., Rees et al., 1986; Killeen et al., 1995; Förster et al., 2008 and Förster et al., 2011). In contrast to
221 KEOPS, the higher latitude station Longyearbyen is located close to or even poleward of the dusk cell's focus,
222 so that the cross-polar cap circulation of the neutral thermospheric air dominates.
223
224

225   **Figure 1: CHAMP observations over Longyearbyen during solar maximum 2001-2003. a) All data – ascending (blue)**

226   **and descending (red) averages; b) Summer (May-Aug) and c) Winter (end Oct-early Mar).**

227
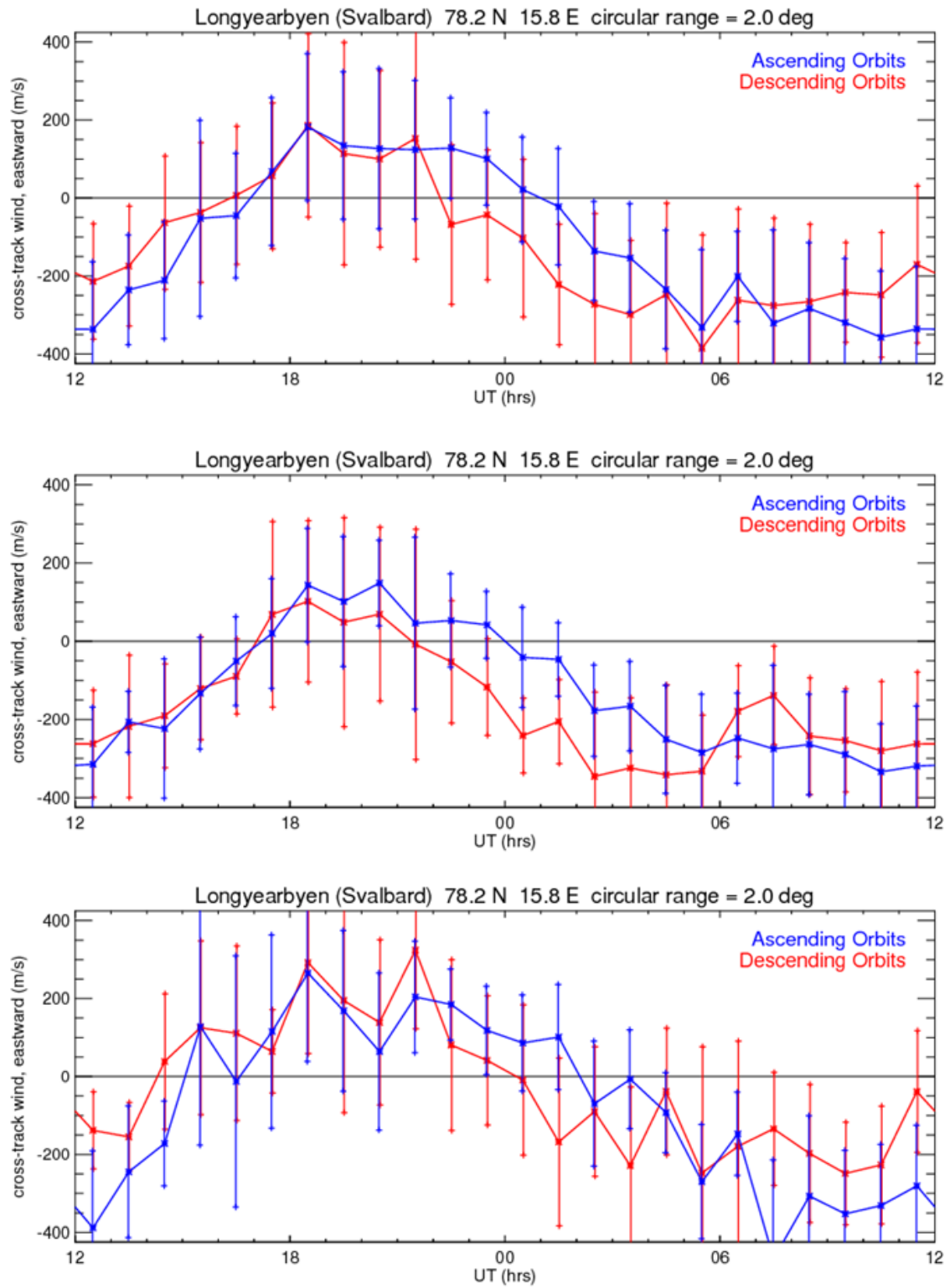
Figure 2: CHAMP observations over KEOPS during solar maximum 2001-2003. a) All data – ascending (blue) and
descending (red) averages; b) Summer (May-Aug) and c) Winter (end Oct-early Mar).
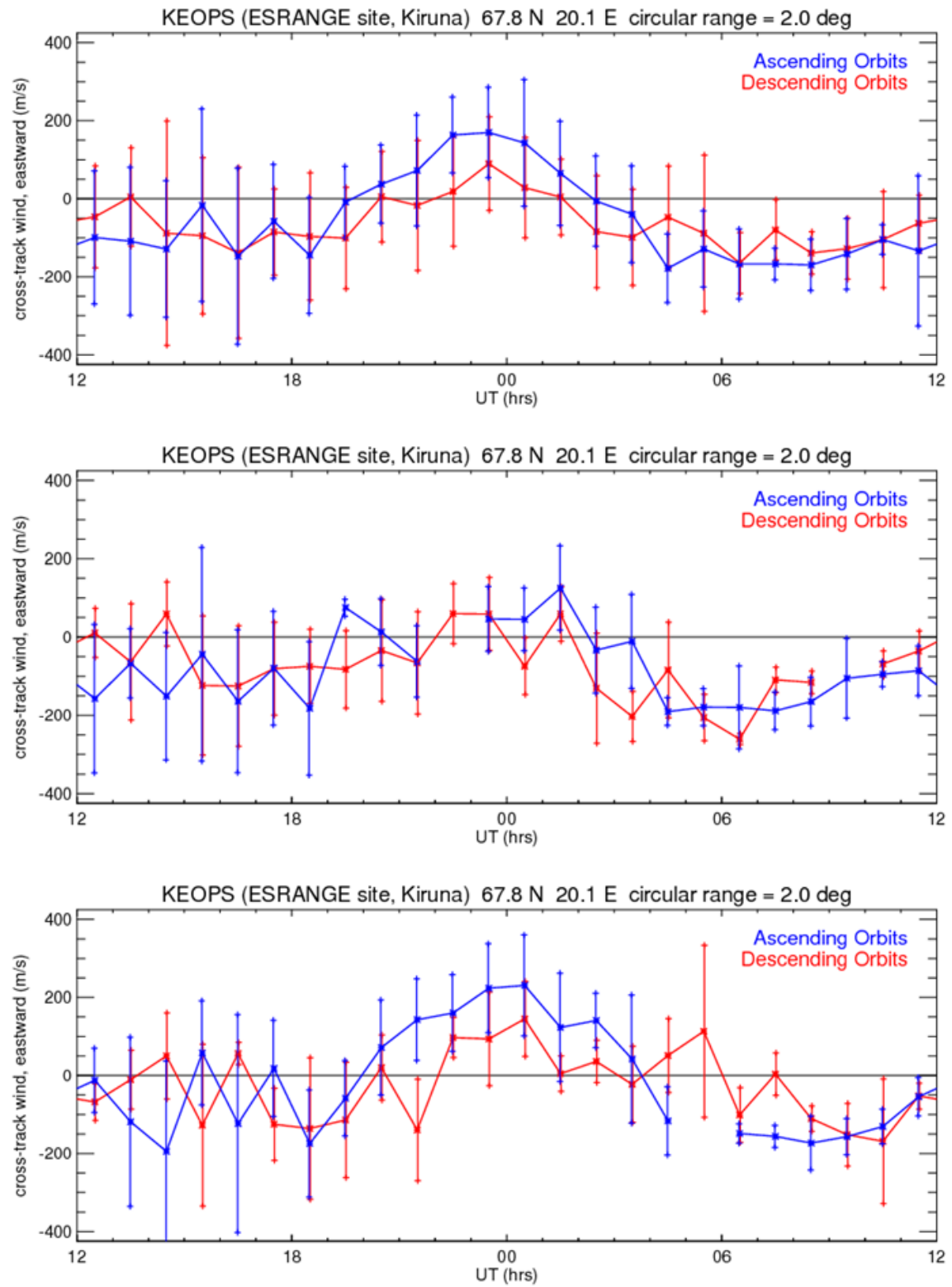
230 Figures 1b and 1c repeat the statistical plot of Fig. 1a for Longyearbyen for the years 2001-2003 with high solar

231 activity, but confined to the winter and summer months, respectively. Similarly for Figures 2b and 2c for

232 KEOPS. The statistical significance is therefore reduced, in particular for the KEOPS station, but seems to be

233 still sufficient. The winter recordings (Fig. 1c and 2c) during nighttime hours can directly be compared with the

234 FPI observations (Figs. 6 and 7).

235

236 The principle behaviour of the Longyearbyen and KEOPS eastward wind component is similar to that for the

237 full year coverage, but there are also obvious seasonal differences. The wind component amplitudes, in

238 particular the eastward maxima, are smaller during summer compared with the winter months, while the phases

239 are almost the same. The statements about the variance of the eastward/westward wind component for both

240 stations that have been made with respect to the full year statistics in Fig. 1 hold also for both winter and

241 summer plots, maybe with slightly larger values for the winter months.

242

243 The ascending and descending orbits are analyzed separately in their statistical behaviour (blue and red lines and

244 vertical bars, respectively), and show distinct differences. This points to the problem of co-alignment of the

245 ascending and descending orbital tracks (despite the simple sign flip). The small offset of ~2.7° from a strict

246 polar orbit of the satellite causes some deviation from the east/westward pointing of the cross-track

247 measurements. At low to mid-latitudes, the deviation from purely geographically eastward direction corresponds

248 in good approximation to this colatitude angle of the satellite's inclination $\beta \approx 2.7°$, but at high latitudes and in

249 particular near the poles it can deviate considerably. This non-alignment angle α (deviation from purely

250 eastward) can be estimated in dependence on the observer's colatitude θ with spherical angle relations using a

251 simplified spheric geometry of the Earth as in Eq. (1).

252

$$\alpha = \arcsin\left(\frac{\sin\beta}{\sin\theta}\right) \tag{1}$$

253

254 Using the geographic coordinates of the observatories in Table 1, one gets an α-angle of 7.2° and 13.3° for

255 KEOPS and Longyearbyen, respectively. The angular difference (2·α) between the two one-component cross-

256 track wind measurements of the ascending and descending orbital tracks is already considerable for the most

257 northward station at Longyearbyen and this offset can be noticed in, for example, Figure 1a as an offset between

258 the wind averages for ascending and descending orbital tracks during certain intervals, where the wind

259 component perpendicular to the zonal wind direction, i.e. the north-south meridional wind, is large. This is

260 obviously the case for the nighttime hours between 23–05 LT and the daytime hours between ~10–17 LT for

261 Longyearbyen and for a few nighttime hours between 23–03 LT for the KEOPS FPI station.

262

263 If the FPI technique, in particular the tri-static measurements for certain periods (Aruliah et al.,2005; Griffin et

264 al., 2008), allows the determination of specified neutral wind directions, one might consider comparing the wind

265 magnitudes for the descending and ascending orbital tracks separately for an eastward $\pm\alpha$ orientation,

266 respectively. Here, one should note, that at an observation point with an even higher geographic latitude (ideally

267 at ~86.2° geographic latitude, where the two branches of one-component observations would be perpendicular

268   to each other) it would in principle be possible to derive the full thermospheric horizontal wind vector from the

269   cross-track accelerometer measurements. This is, strictly spoken, valid in a statistical mean with characteristic

270   times of a few days, i.e. with the repetition period of ascending and descending orbits over one and the same

271   high-latitude location.

272

273   The meridional component is much larger than the zonal one during considerable periods of the nighttime

274   observation. So, to minimize the error in comparing the neutral wind magnitude, it would be better to compare

275   the full vectors. Already a small error of the measurement orientation could make a large effect on the relatively

276   small eastward wind component, which could lead us to wrong conclusions about the characteristics of the

277   differences between FPI and CHAMP accelerometer measurements. The offset between the geographic and

278   geomagnetic coordinates allows the construction of the full horizontal vector plots as statistical averages taken

279   over a period of at least 131 days of CHAMP's precession period in order to cover all local times. This

280   statistical mapping is limited to magnetic latitudes poleward of about $> 60°$ for both hemispheres (cf. Förster et

281   al., 2008).

282

283   **Figure 3: Geometry illustrating the projection of FPI look direction horizontal wind components onto the CHAMP**

284   **cross-track direction for the ascending and descending tracks.**

285
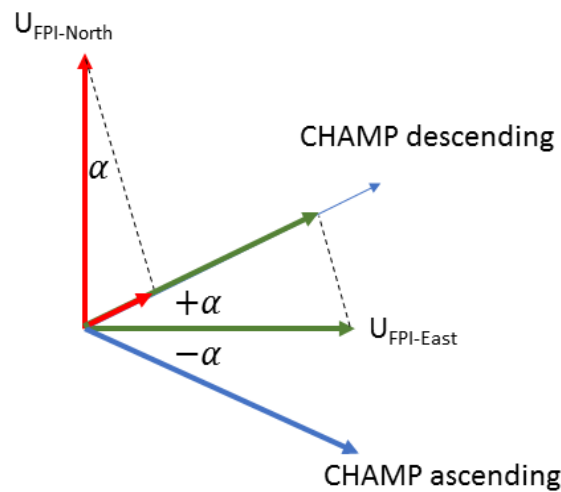
286   Figure 3 illustrates the projection of the horizontal wind component from the north and east FPI look directions

287   onto the cross-track direction of the CHAMP ascending direction. It also illustrates how the average of the

288   CHAMP ascending and descending winds gives the zonal wind component. The projections of the FPI wind

289   vectors onto each of the ascending and descending directions are used later in determining the ratio of the

290   CHAMP/FPI wind magnitudes (see section 5.2 Figure 10).

Figure 4: CHAMP observations over Longyearbyen during solar minimum 2005-2007. a) All data – ascending (blue) and descending (red) averages; b) Summer (May-Aug) and c) Winter (end Oct-early Mar).
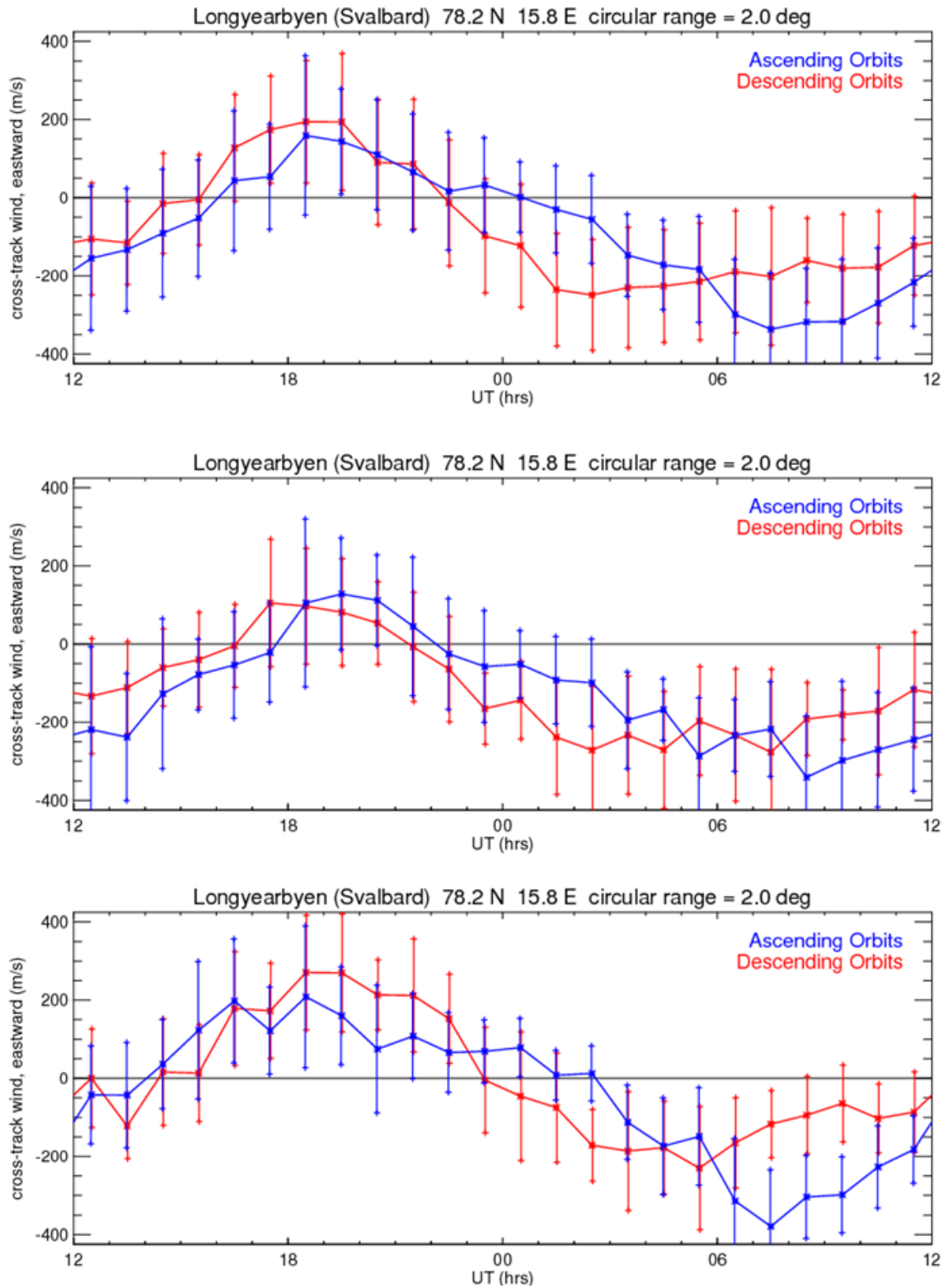
 Figure 5: CHAMP observations over KEOPS during solar minimum 2005-2007. a) All data – ascending (blue) and
 descending (red) averages; b) Summer (May-Aug) and c) Winter (end Oct-early Mar).
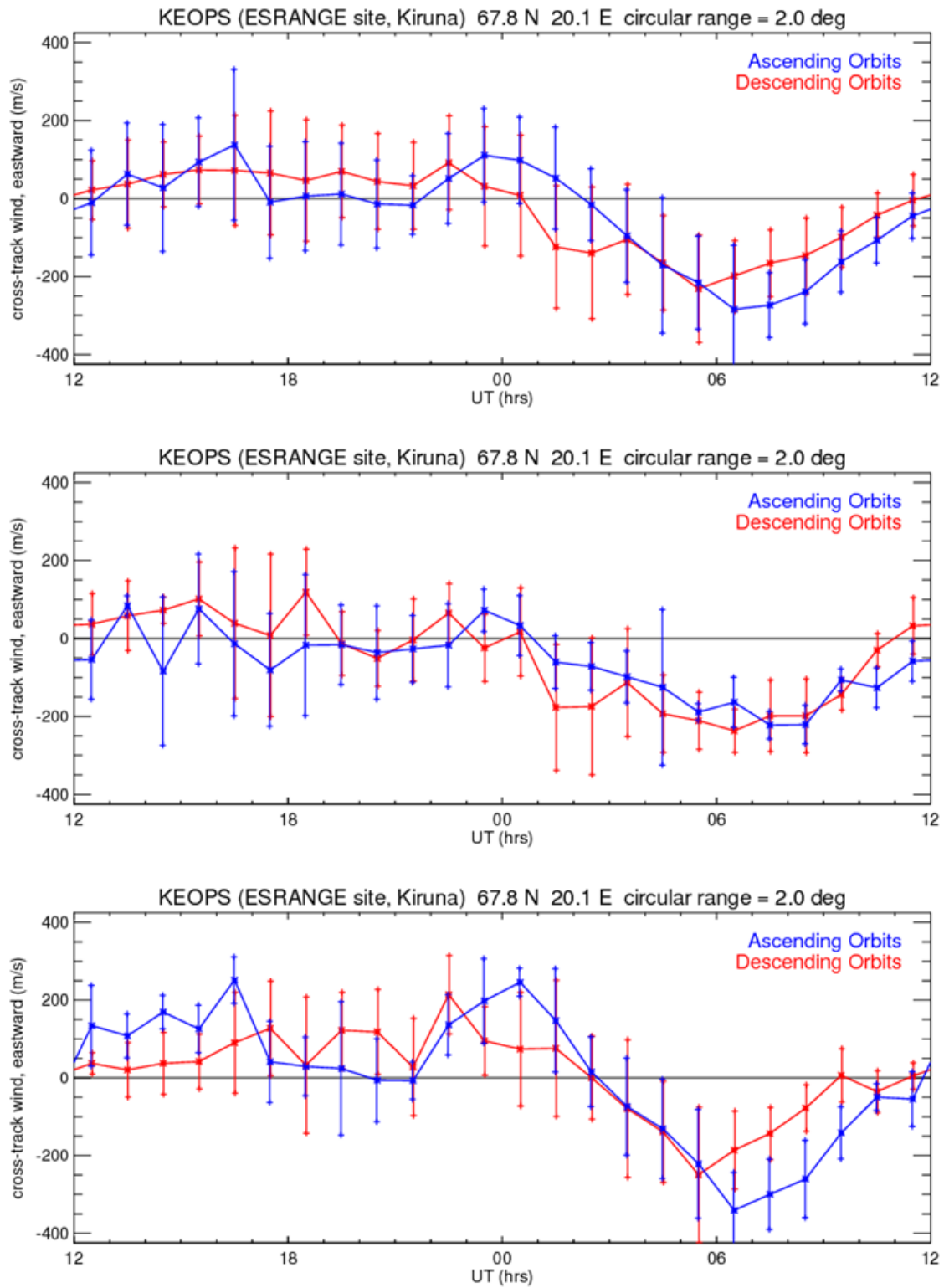
297   Figures 4 and 5 show the corresponding plots to Figs. 1 and 2, but now for low solar activity conditions during

298   the years 2005-2007. They reveal some differences as, e.g., generally smaller amplitudes and different wind

299   phases. Here, the zonal wind above KEOPS seems to point eastward during most times of the day except the

300   morning hours 04–11 LT.

301

302   **5.2 FPI average winds**

303   The average winds observed at Kiruna and Longyearbyen are presented in Figures 6 and 7. Local Time is 1 hour

304   ahead of Universal Time for both sites. The format of these figures is that the plots 6a, 6c, 7a and 7c show the

305   average zonal wind component, comparing observations from the volumes to the East and West of the site. The

306   plots 6b, 6d, 7b and 7d show the average meridional wind component from the volumes observed to the North

307   and South. The full set of cardinal direction measurements, are presented to provide a context for the

308   comparison with the zonal wind measurements made by CHAMP, especially since the CHAMP y-axis is only

309   roughly zonal. The standard error of the mean ε is added as an error bar to the FPI East and North data, where ε

310   $= \sigma/\sqrt{(N-1)}$, σ is the standard deviation and N is the number of data points. The standard errors of the mean

311   (rather than the standard deviations) demonstrate the distinctly different trends in the winds observed in the

312   volumes to the East and West of the sites, i.e. the meso-scale structure of the high-latitude thermosphere.

313   The periods of data cover the winter months of 2001-2003 and 2005-2007 to match with the CHAMP datasets.

314   The FPIs cannot measure winds during cloudy periods owing to the scatter of light by the clouds, and are only

315   able to observe the emission during the hours of darkness. Thus the observing days cannot be identical to the

316   dates when CHAMP passed overhead of the two sites. Longyearbyen has 24 hours of darkness during the

317   months of November to January, so there are nearly 24 hours of observations, but the longest period of darkness

318   at Kiruna is around 18 hours in mid-winter. CHAMP, meanwhile, is able to provide a full 24 hours of

319   observations from drag measurements.

320   There are consistent differences in the winds observed to the geographic East and West, or to the North and

321   South. This is understandable because the Kiruna site is, on average, at the equatorward edge of the auroral oval,

322   while Longyearbyen is mostly in the polar cap, though towards the poleward edge of the auroral oval. The

323   expansion and contraction of the auroral oval during an active period means that the northern half of the FPI

324   field-of-view can be very different from the southern half. In fact, Emmert et al. (2006) have shown that high

325   latitude neutral winds are better ordered in geomagnetic coordinates of magnetic latitude and magnetic local

326   time than in geographic coordinates and universal time. The AACGM geomagnetic coordinates shown in Tables

327   1 and 2 give an indication of how different are the magnetic latitudes for the East and West look directions.

328   Figure 6 shows average zonal and meridional winds from FPI observations at Longyearbyen. Figs 6a and 6b

329   show solar maximum years (2001-2003), while Figs 6c and 6d show solar minimum years (2005-2007). Figs 6a

330   and 6c show the zonal winds to the East and West using the convention of +East, while Figure 6b and 6d shows

331   the meridional winds to the North and South, using +North. The average standard deviations σ are ± 103 ms^{-1}

332   and ± 64 ms^{-1} for the solar maximum zonal and meridional winds, respectively.

333

334   **Figs 6a and b show solar maximum (2001-2003) FPI winter average wind components at Longyearbyen for**

335   **geomagnetically quiet conditions** $(0 \leq Kp < 2\text{-})$**. a) Zonal and b) meridional average winds and the standard errors of**

336   **the mean are plotted. North and East are purple lines, while South and West are light blue**.

337
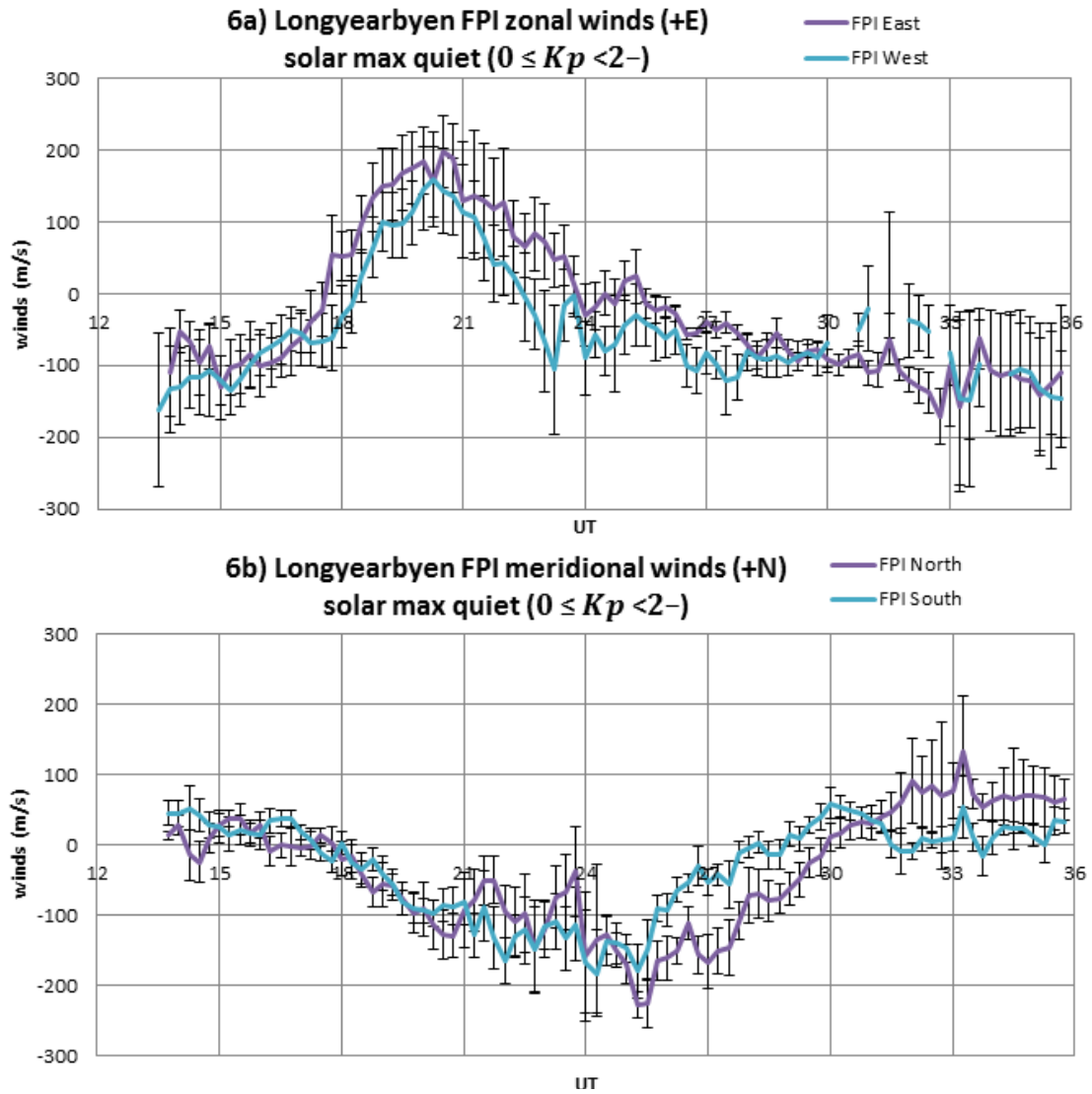
338   **Fig 6c and d show solar minimum (2005-2007) FPI winter average wind components at Longyearbyen for**

339   **geomagnetically quiet conditions** ($0 \leq \mathrm{Kp} < 2\text{-}$)**. a) Zonal and b) meridional average winds and the standard errors of**

340   **the mean are plotted. North and East are purple lines, while South and West are light blue**.

341

342
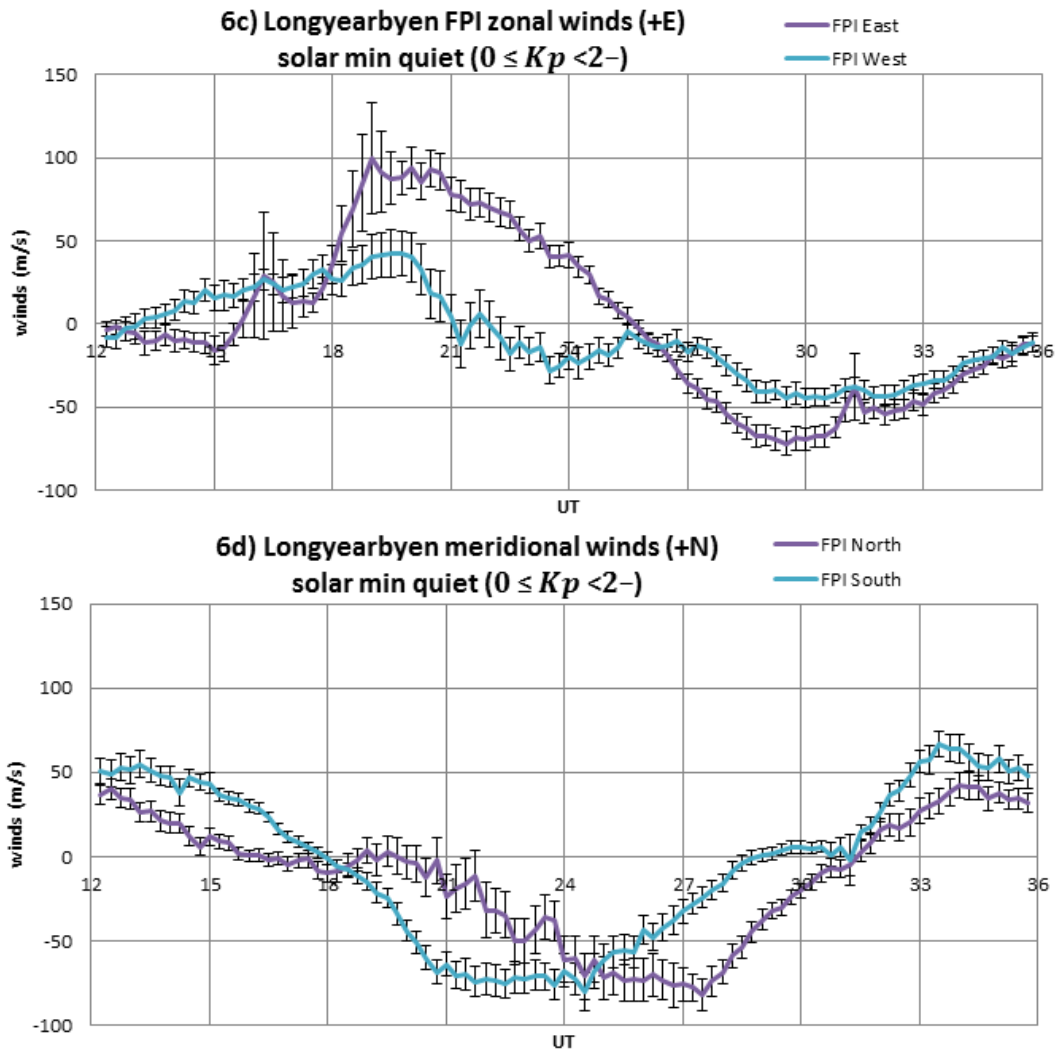
343   Longyearbyen is just within the polar cap. The winds are predominantly antisunward despite the geomagnetic

344   activity level, since this is the direction for both the pressure gradient and ionospheric convection. As a result,

345   Longyearbyen observations are a somewhat less obvious indicator of ion-neutral coupling behaviour than

346   observations at KEOPS in the period 1800-2100 UT. The Longyearbyen solar maximum (2001-2003) winter

347   winds (day numbers 300-65), during geomagnetically quiet conditions ($0 \leq Kp < 2-$) are shown in Figures 6a

348   and 6b. The zonal winds (Figure 6a) show westward winds before 1800 UT and then eastward winds for ~6

349   hours which then turn westward. The maximum wind speed is about 200 ms^{-1} eastward between 1800-2400 UT.

350   The meridional winds (Figure 6b) are slightly northward before 1700 UT, then turn southward until 0600 UT,

351   and return northward. The maximum speed is about 200 ms^{-1} southward at about 0100 UT. The standard errors

352   of the mean are around ±30 ms^{-1}, however the values vary systematically through the night. Between 1800-2100

353   UT the standard error is around 3 times larger than between 0300-0900 UT when it is very small.

354   Figures 6c and 6d show the Longyearbyen FPI winds for clear nights during winter (DOY 300-65) 2005-2007,

355   geomagnetically quiet conditions ($0 \leq Kp < 2-$). There is a full 24 hours of observations in this dataset, and the

356   extreme quiet of this solar minimum period has provided a large number of observations for this category. The

357   antisunward flow appears clearly. There is a strong phase lag between the observations to the North and South.

358   This is puzzling because it cannot be explained in terms of ordering high latitude winds in geomagnetic

359   coordinates. This category is for the most geomagnetically quiet conditions possible: solar minimum during a

360   prolonged solar minimum, and the lowest Kp values. Under these conditions the geographic coordinate system

361   under which the solar flux heating operates, should be the most appropriate. The average standard deviations are

362   ±55 ms^{-1} and ±47 ms^{-1} for the zonal and meridional winds, respectively. The standard errors of the mean are

363   very small, averaging less than ±10 ms^{-1}, though again there is a clear systematic UT-dependent trend. Between

364   2100-0300 UT the standard error of the meridional wind is about 2-3 times larger than at other times. Between

365   1500-2000 UT the zonal wind standard error becomes considerably larger.

366

367 **Fig 7a and b show solar maximum (2001-2003) FPI winter average wind components at KEOPS for geomagnetically**

368 **quiet conditions** $(0 \leq \mathrm{Kp} < 2\mathrm{o})$**. a) Zonal and b) meridional average winds and the standard errors of the mean are**

369 **plotted. North and East are purple lines, while South and West are light blue**.

370

371

7c) KEOPS FPI zonal winds (+E) solar min, quiet ($0 \leq Kp < 2-$)

7d) KEOPS FPI meridional winds (+N) solar min, quiet ($0 \leq Kp < 2-$)

375
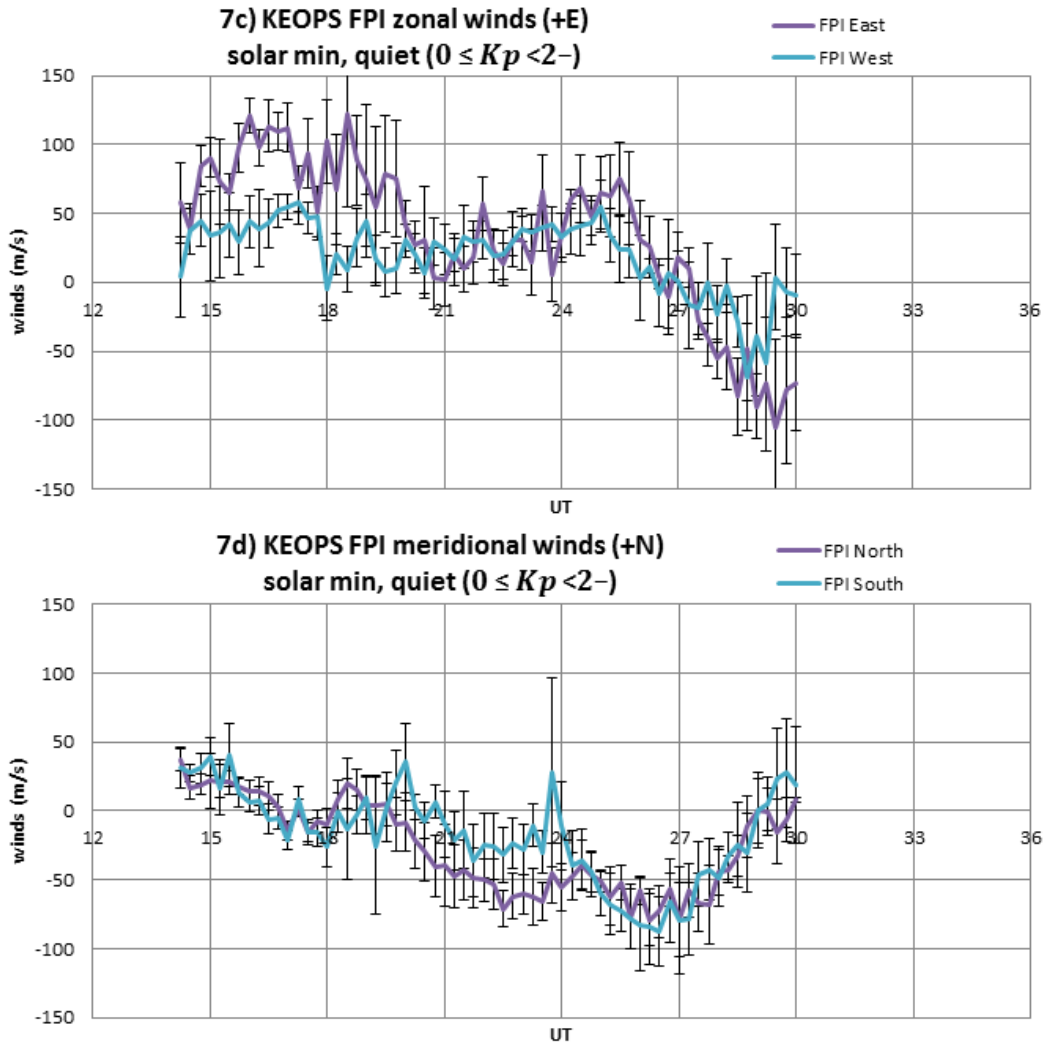
376   Figure 7 shows the KEOPS FPI winds for clear nights during winter (DOY 300-65) during geomagnetically

377   quiet conditions. The general diurnal trends are similar for both solar maximum (Figs 7a, b) and minimum (Figs

378   7c, d). The solar minimum data range is $0 \leq Kp < 2$-, but it was necessary to increase the geomagnetic activity

379   spread for the solar maximum data to improve the statistics, so Figures 7a, b show $0 \leq Kp < 2o$. The meridional

380   winds show antisunward flow that is predominantly driven by the pressure gradient from dayside EUV heating,

381   resulting in fairly weak southward winds reaching a maximum value of nearly 100 ms^{-1}. The standard errors of

382   the mean are around ±10-15 ms^{-1}. The zonal winds are eastward before 1800UT, reaching a maximum speed of

383   a few 10s ms^{-1}. After 1800 UT the zonal winds turn westward for a few hours and back eastwards around

384   2100UT. Between 2100-0300 UT the zonal winds reach their maximum speed of up to 80 ms^{-1} before turning

385 westward again. The zonal winds are more variable, and their standard errors of the mean are slightly larger than

386 for the meridional winds, averaging 16 ms^{-1}.

387 The few hours of westward flowing zonal winds during 1800-2100 UT are particularly interesting (Figs 7a and

388 7c). The westward flow indicates that the winds are briefly under the influence of the clockwise dusk cell of

389 ionospheric convection. Through collisions between the ions and neutral gas, momentum is transferred to the

390 neutrals, which diverts them from the direction of the pressure gradient driven anti-sunward/eastward flow. The

391 action of the centrifugal force balancing the Coriolis force keeps the winds entrained in the cell (Fuller-Rowell

392 and Rees, 1984). As the KEOPS site passes under the region of the Harang Discontinuity (Harang, 1946), the

393 FPI West zonal winds turn back to eastward about 40 mins after the FPI East zonal winds. This is because the

394 KEOPS FPI East observing volume is a horizontal distance of 480 km away from the FPI West volume (note

395 that the distance between the viewing volumes depends on the altitude of the 630 nm emission). However, note

396 that at the latitude of KEOPS, the time taken for the Earth to rotate through a distance of 480 km is 46 mins. The

397 difference between 40 min and 46 min is partly due to the difference in magnetic latitude. It is also due to the

398 Harang Discontinuity being dependent on the IMF B_y orientation, resulting in a smearing out of the MLT

399 interval.

400 Figures 7c and 7d show the KEOPS FPI winds for clear nights for the years 2005-2007 during winter (day

401 numbers 300-65), geomagnetically quiet conditions (0 ≤ Kp < 2-). These years were during the unusually

402 extended solar minimum of the last solar cycle when the solar flux levels were extremely low, and observations

403 of aurora were rare. Consequently the plasma density was smaller, and the thermosphere was more compressed,

404 resulting in smaller neutral densities at a given height. Under these conditions the ion drag driver is less

405 efficient, and the pressure gradients, together with the Coriolis and centrifugal forces, play a larger role. Thus,

406 although the trends are similar to the solar maximum winds; the zonal winds are strongly eastward throughout

407 the evening sector. There are no westward zonal winds until after 0300 UT, and generally the wind amplitudes

408 are smaller. The maximum meridional wind is about 80 ms^{-1} southward around 0300 UT. The maximum zonal

409 winds are seen to the East, and these are around 100 ms^{-1} eastward in the evening sector and start to increase

410 westwards towards 100 ms^{-1} by 0600 UT. The average standard errors of the mean are around ± 20 ms^{-1}, which

411 are larger than for solar maximum conditions.

412 The general trends seen in the northern winter geomagnetically quiet CHAMP zonal winds (Figures 1-2, and 4-

413 5) are also seen in the FPI winds (Figures 6-7). The phases match well for both sites, however, there is a

414 considerable difference in magnitude. The next two figures (Figures 8-9) show direct comparisons of CHAMP

415 and FPI winds along the cross-track direction for moderately active conditions (2$^-$ ≤ Kp < 4$^+$). There is a lot of

416 modelling effort into studying the active ionosphere-thermosphere, which makes this comparison useful. In

417 particular it is relevant to the argument in section 6.4 where CHAMP and FPI neutral winds are compared with

418 typical ion velocities actively observed by ground-based radars at high latitudes.

419

420 **Fig 8 Longyearbyen (Svalbard) winters 2001-2003, 2- ≤ Kp < 4+: average zonal winds measured using CHAMP and**

421 **FPI, including standard errors of the mean. These are compared with FPI winds observed by the University of**

422 **Alaska in 1980, and the HWM93 model winds.**
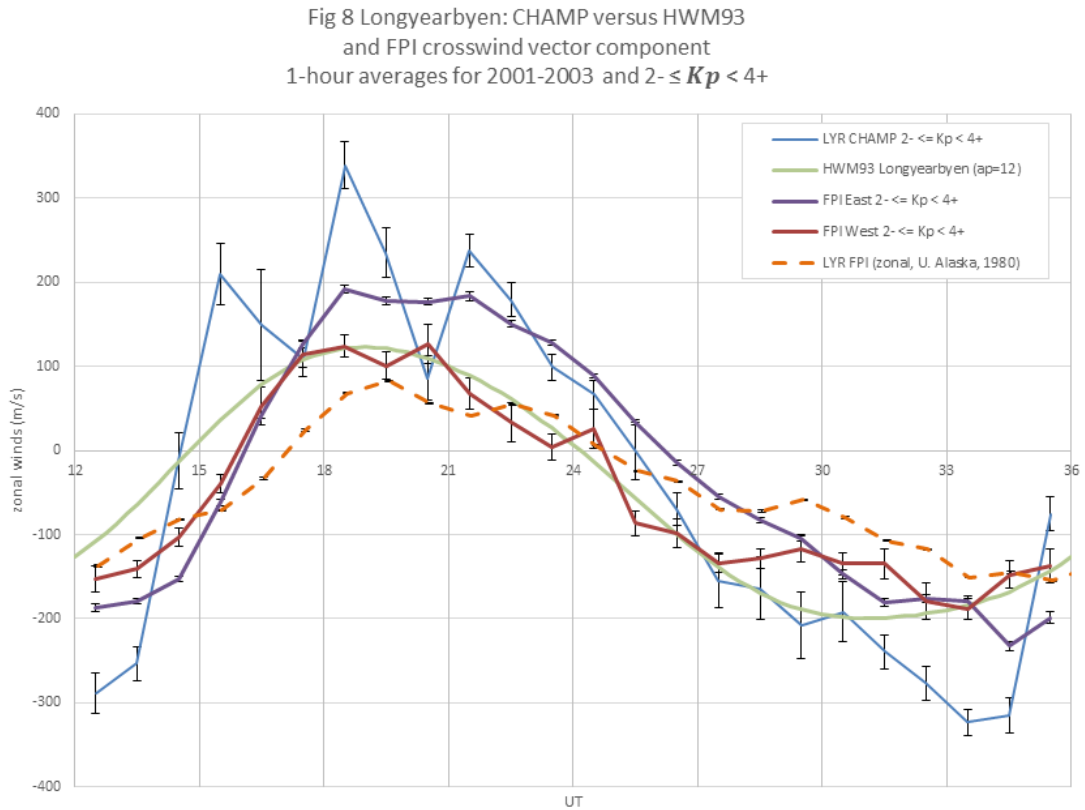
423 Figure 8 is a direct comparison between CHAMP cross-track winds at Longyearbyen and several different

424 sources. The winds represent moderately active conditions ($2^- \leq$ Kp $< 4^+$) during winter months (DOY 300-65)

425 for solar maximum years. The HMW93 model conditions are for the 31st December with ap = 12 (Kp = 3-);

426 F10.7 =150; height 400 km (Hedin et al., 1996). At Longyearbyen there can be 24-hour coverage by the FPI

427 owing to continual darkness between November-January. The direct comparison is made by projecting the

428 components of the FPI and HMW93 (Hedin et al., 1996) wind vectors along the CHAMP ascending and

429 descending cross-track directions using $\alpha = \pm 13.3°$. CHAMP cross-track winds and UCL Longyearbyen FPI

430 observations are averages for 2001-2003 (a failure occurred in the rotating mirror mechanism in late December

431 2003 so CHAMP 2004 data were not included). The data are then the averages of the ascending and descending

432 components to give a zonal wind.

433

434 FPI wind values taken from Figure 9 in the paper by Hedin et al. (1991) are also plotted. These values are

435 measurements from the University of Alaska FPI that collected Longyearbyen data in 1980, 1981 and 1983. The

436 aim is to demonstrate that the FPI technique of measuring Doppler shifts gives consistent results, which is

437 discussed in section 6.2. The U.Alaska FPI winds were an average of the East and West look directions, justified

438 by the assumption of a uniform horizontal wind field over the field of view. This was a common practice at that

439 time owing to a) the assumption of a large molecular viscosity of the thermosphere which reduces wind shear,

440 and b) the longer exposure times of the earlier FPIs (6-12 minutes) which used photomultipliers with
441 piezoelectrical scanning of the FPI etalon gap size in order to view the full Free Spectral Range (Deehr et al.,
442 1980). The UCL FPIs were amongst the first FPIs to use fixed gap etalons to image the full FSR onto a 2D array
443 of pixels. This allowed shorter exposure times, and a rapid cycle of look directions, which consequently
444 revealed mesoscale spatial and temporal structures of the order of a few 100 km horizontally and minutes (e.g.
445 Aruliah and Griffin, 2001, Aruliah et al, 2005). During the 1980s and 1990s we used state-of-the-art UCL
446 designed and built Imaging Photon Detectors (McWhirter et al., 1982). Astrocam Antares cameras replaced the
447 IPD in the Svalbard FPI from 1998, and in the KEOPS 630 nm FPI in 2002. However, these cameras had the
448 disadvantage of slow readout times which were essential for the best noise performance and so time resolution
449 was compromised. In 2003 the first Electron Multiplying CCDs revolutionised low light level imaging. These
450 cameras combined superior signal to noise ratio with very fast readout times. The first one was put into service
451 at KEOPS in 2003, followed by Svalbard in 2005 (McWhirter, 2008). The huge advancement over the last 30
452 years in low light detectors has allowed atmospheric gravity wave observations using exposure times as little as
453 10 seconds at auroral latitudes (Ford et al., 2007). Note that the upgrade of the detector is to improve the photon
454 sensitivity which reduces the error of measurement. It does not change the calibration of the wind speeds.

455 Any changes of etalon required re-calibration of the measured Doppler shift to calculate winds, as discussed in
456 section 6.2. The KEOPS FPI used a 10 mm etalon gap up to January 2002, when it was replaced with an 18.5
457 mm gap etalon. Then in January 2003 a 14 mm etalon was put in, which has been there until the present time.
458 For the Longyearbyen FPI there was a 14 mm etalon until April 2005, which was replaced with an 18.5 mm
459 etalon from September 2005 until the present time.

460

461 All sources show generally similar phases, with peak eastward winds in the evening sector, between 18-24UT
462 and westward winds in the morning sector, between 06-12UT, as expected for anti-sunward flows. Table 2
463 shows that the AACGM MLT for Longyearbyen is about 2.4 ($\pm$ 0.8 for the East and West volumes) hours
464 ahead, so magnetic midnight is approximately at 21.6 UT. The standard errors of the mean are plotted for all
465 data. The U.Alaska Longyearbyen FPI standard deviations are around $\pm$ 150 ms^{-1}, which are similar to the UCL
466 FPI. For the purposes of comparison, a standard error of $\pm$ 30 ms^{-1} is plotted for the U.Alaska FPI data, similar
467 to the average UCL FPI standard error. It was noted in the Hedin et al (1991) paper that for both hemispheres,
468 the average high latitude winds from the FPIs at Sondrestrom, Longyearbyen and College in the northern
469 hemisphere, and Mawson in the southern hemisphere, showed a systematically smaller diurnal variation than the
470 DE 2 satellitedata. The more recent measurements from CHAMP and the UCL FPI are clearly typically different
471 in magnitude, but consistent with the trend noticed by Hedin et al (1991). The diurnal amplitude of the UCL
472 zonal winds is about 170 ms^{-1}, and for the U.Alaska winds is about 125 ms^{-1}. The CHAMP zonal winds are the
473 largest in magnitude, with a diurnal amplitude of around 300 ms^{-1}.

474 The average of the monthly F10.7 fluxes is 184 for the winter periods Nov-Feb of 1980-81, 1981-82 and 1983-
475 84, and 160 for the winters of 2001-2003. Yet despite the higher average solar flux in 1980, the UCL FPI zonal
476 wind magnitudes have a significantly larger amplitude than the U.Alaska zonal winds. Closer inspection of the 3
477 winter periods of 2001-2003 shows a spike in the average monthly F10.7 for November 2001-February 2002
478 (i.e. <F10.7> is 214 for Nov-Feb 2001-2002; 145 for Nov-Feb 2002-2003; and 123 for Nov-Dec 2003) which

479   may account for the 3 winter average UCL FPI winds being larger than for U.Alaska. The geomagnetic activity

480   levels are similar, averaging Kp values in the range 3⁻ to 3° for all three winters. These are interannual and inter-

481   solar cycle discussions for a later paper.

482

483   **Fig 9 Comparison of CHAMP and FPI measurements of KEOPS zonal average winds to the FPI East and West**

484   **volumes, including standard errors of the mean, for winters 2001-2003. These are compared the HWM93 model**

485   **winds.**

486

487
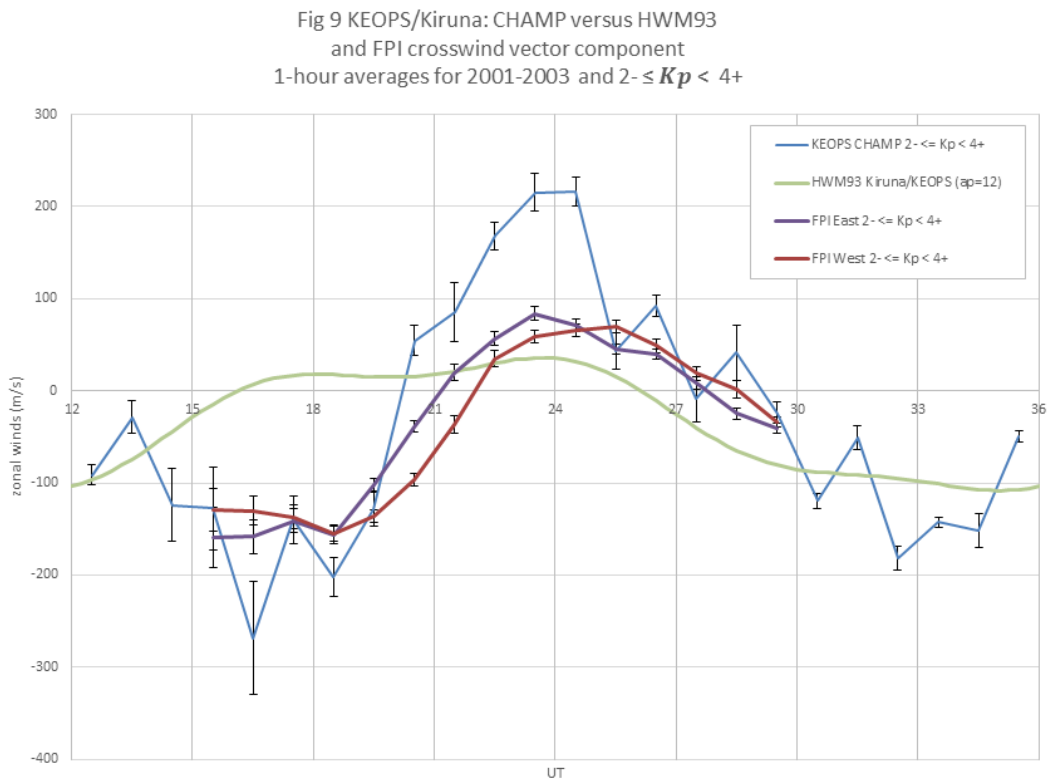
488   Figure 9 shows a comparison of the CHAMP zonal winds against the UCL FPI winds at Kiruna/KEOPS for the

489   solar maximum winters of 2001-2003. The FPI and CHAMP data are selected for moderately active conditions

490    $(2^- \leq$ Kp $< 4^+)$ as in Figure 8. At Kiruna the hours of darkness are between 15-06UT for the period November-

491   January. The direct comparison is made by taking the component of FPI and HMW93 (Hedin et al., 1996) wind

492   vectors in the CHAMP cross-track direction using $\alpha = \pm\,7.2°$. The UCL FPI average zonal winds for $2^- \leq$ Kp

493   < 4+ are shown separately for the East and West look directions. There is a smaller difference between these

494   look directions than for the Longyearbyen zonal winds. The evening winds for moderately active solar

495   maximum conditions are around -150 ms⁻¹ (westward), and reach a peak of around 70 ms⁻¹ (eastward) in the

496   midnight sector. The AACGM MLT for Kiruna is about 1.9 (± 0.3 for the East and West volumes) hours ahead,

497   so magnetic midnight is approximately at 22.1 UT, which is the time separating the period of the evening

498 eastward electrojet and the morning westward electrojet in magnetic local time coordinates. The behaviour of
499 the zonal winds shows strong ion-neutral coupling for these moderately active conditions, so that there is a
500 semidiurnal variation representative of the twin cell ionospheric convection pattern at auroral latitudes. This is
501 in addition to the day-night diurnal variation of winds driven by the pressure gradient.

502 The phase of the CHAMP zonal winds is in good agreement, but the amplitude is considerably larger. The peak
503 evening wind reaches -200 ms^{-1} (westward) and 200 ms^{-1} (eastward) by 02 UT. What is particularly interesting
504 about this comparison is the difference between the CHAMP and FPI winds in the period 15-20 UT. The
505 CHAMP winds are considerably less westward, and are more similar to FPI average zonal winds for
506 geomagnetically quieter conditions at solar maximum, as shown in Figure 7a. The large standard error of the
507 mean during the period 15-20 UT shows how sensitive the winds are to ion drag within the dusk cell.

508 Figure 10a shows the histogram of the frequency distribution of the ratios of CHAMP/FPI 1-hour averaged
509 cross-track zonal wind magnitudes from Figures 7 and 8. Figure 10b shows the UT dependence. The
510 Longyearbyen ratios cluster in the range 1.0 - 2.5, while the Kiruna ratios are far more widely spread. Overall
511 there is a general trend for the satellite wind magnitudes to be larger by a factor of 1.5 - 2.0, with median values
512 of 1.7 for Longyearbyen (24 hours coverage) and 1.3 for Kiruna (1530-0530 UT coverage). There does not seem
513 to be any clear pattern when the UT-dependent frequencies of the ratios are plotted in Fig 10b, except for a
514 tendency for the more extreme ratios to occur during the midnight period, when the 630 nm emission is weakest,
515 and the FPI winds have the largest error bars. Even if the midnight measurements are excluded, there is a wide
516 range of values generally greater than 1.0.

517

Fig 10a, b Frequency distribution of the ratios of CHAMP/FPI one-hour averaged zonal wind magnitudes observed in the winter period for solar max under moderately active conditions (2- ≤ Kp < 4+) for Longyearbyen (blue) and KEOPS (red). Fig 10a shows the frequency distribution of the CHAMP/FPI ratios, and Fig 10b shows the UT dependence of the ratios.
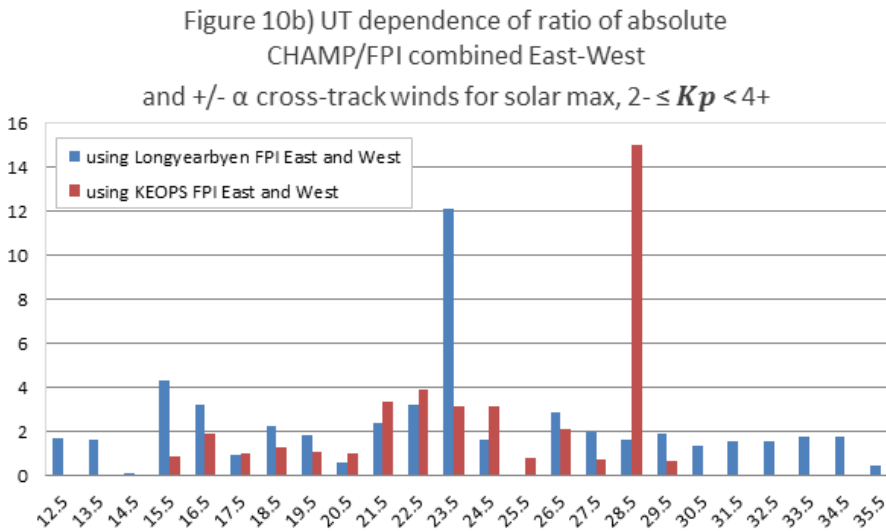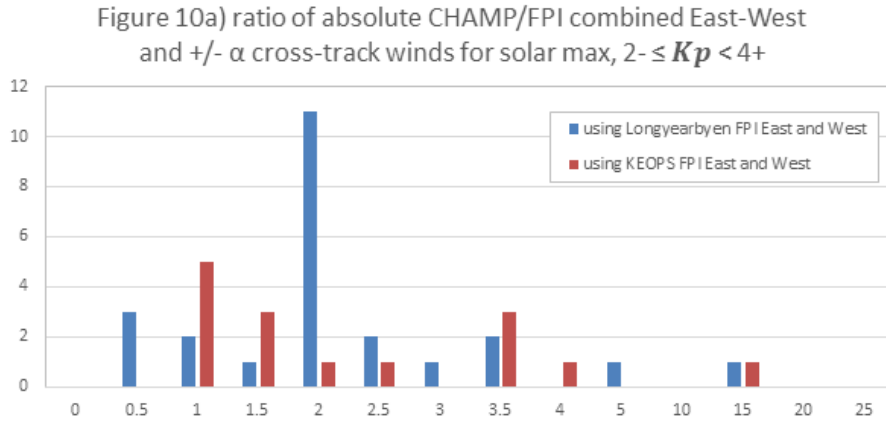
6. Discussion

We have shown that there is a similar phase, but a considerable difference between the average zonal wind magnitudes measured by the CHAMP satellite and the ground-based FPIs for a polar cap and auroral site during northern winter months. Our premise is that the large molecular viscosity of the upper thermosphere should minimise any vertical structure in the winds above around 250 km altitude. The difference in wind magnitudes could have various explanations. It could be that A) we are mistaken about the vertical structure of winds; or B) that there is a problem with the scaling of the two methods of measurement; or C) the measurement procedures introduce differences, e.g. in-situ versus remote integration; comparison of different spatial and/or temporal resolutions. There may be other, unexpected, reasons for the mainly amplitude differences in the measurements.

531 With respect to hypothesis A: the CHAMP satellite average cross-track winds are of a similar magnitude to the
532 original GOCE satellite winds (Liu et al., 2016 and Visser et al., 2019), and to the UCL CMAT2 model
533 simulations. However, while the CHAMP satellite altitude was between 350-400 km, the GOCE satellite had an
534 unusually low altitude around 250 km, which was close to the FPI 630 nm emission peak altitude. The CMAT2
535 winds are typical of values from other GCMs, which were largely calibrated against measurements by satellites
536 in the 1970s and 1980s, in particular the DE-2 satellites. Killeen et al (1984) found a good agreement between
537 the FPI at Longyearbyen (then called the University of Ulster FPI, and subsequently the University of Alaska
538 FPI) for observations in December 1981. Though later Hedin et al. (1991) found that on average the satellite
539 wind measurements were larger. The DE-2 satellite measurements were made using the Wind and Temperature
540 Spectrometer (WATS), rather than derived from satellite drag measurements. The DE-2 satellite flew from
541 August 1981 to February 1983, which means that the average monthly F10.7 flux included some of the highest
542 solar flux values of the last 30 years. This may account for why physical and empirical GCMs calibrated from
543 that period have such large wind values. In contrast, the two decades since 2000 have recorded the most
544 sustained and low F10.7 flux levels since the satellite era began. However, it is also possible that the fact that
545 two different methods of satellite measurements gave winds systematically larger than ground-based FPI
546 measurements might support the existence of a vertical structure in the upper thermosphere.

547 With respect to hypothesis B: the satellite drag community are already aware of a scaling issue. Defining the
548 drag coefficient is the largest source of error. Bruinsma et al (2014) had to multiply GOCE densities by a factor
549 of 1.29 to match the real-time High Accuracy Satellite Drag Model (Storz et al., 2005). HASDM uses data
550 assimilation from the orbits of 75-85 inactive payloads and debris over 200-900 km altitude that are tracked by
551 the Space Surveillance Network (SSN) and is considered a benchmark by that community. Recently March et al.
552 (2019), reanalysed thermospheric densities derived from very precise satellite accelerometers and GPS
553 acceleration using high fidelity satellite geometries. The densities for all the spacecraft surveyed were greater
554 than those derived using surfaces defined by flat panels; and more consistent with each other. The CHAMP and
555 GOCE densities were found to be 11% and 9% larger. Although there is no simple link between densities and
556 winds, this re-scaling of densities gives an indication that it may be necessary to scale winds down for the same
557 measured acceleration (see section 6.3 and Eq. 5).

558 With respect to hypothesis C – the assumptions of the FPI and CHAMP measurement techniques are discussed
559 in the following sections 6.1-6.3.

6.1 Considering the molecular viscosity of the upper thermosphere

561 Let us first consider hypothesis A, that the CHAMP and ground-based FPI average zonal measurements are both
562 correct, and that the factor of 1.5-2.0 difference in wind magnitudes is due to the 100-150 km difference in the
563 altitude of the measurements. Conventional fluid dynamics theory predicts that the molecular viscosity is very
564 high in the upper thermosphere owing to the very low particle densities at these altitudes. The viscosity of a
565 fluid determines how resistant it is to shear forces that cause adjacent layers to move at different speeds.
566 Turbulent viscosity dominates the atmosphere below about 100 km, but molecular viscosity dominates the upper
567 atmosphere. The molecular viscosity of the upper thermosphere is very large, and in the CMAT2 model the

568 molecular viscosity η, is given by Eq. (2) (Harris, 2001; Hood, 2018) which is the SI version, based on Dalgarno

569 and Smith (1962) where it is given in units of micropoise.

570
$$\eta = 4.5e^{-5} \times \left(\frac{T}{1000}\right)^{0.71} \tag{2}$$

571 As a consequence of large viscosity, there is little shear between the different altitude layers above ~200 km for

572 both winds and neutral temperatures (hence the name thermosphere representing an iso-thermal behaviour). The

573 issue raised in this paper is that the difference between CHAMP and FPI wind magnitudes is too large to be

574 consistent with the assumption of large viscosity over this range of altitudes.

575

576 **Fig 11 CMAT2 zonally averaged zonal winds for 00UT at December solstice 2008 (solar minimum conditions) to**
577 **demonstrate the effect of drastically reducing the molecular viscosity in order to raise the altitude where winds**
578 **become independent of altitude. The left panel shows isobars for a standard simulation, while the right panel**
579 **represents a simulation where the molecular viscosity is 100 times smaller (from Hood, 2018).**
580
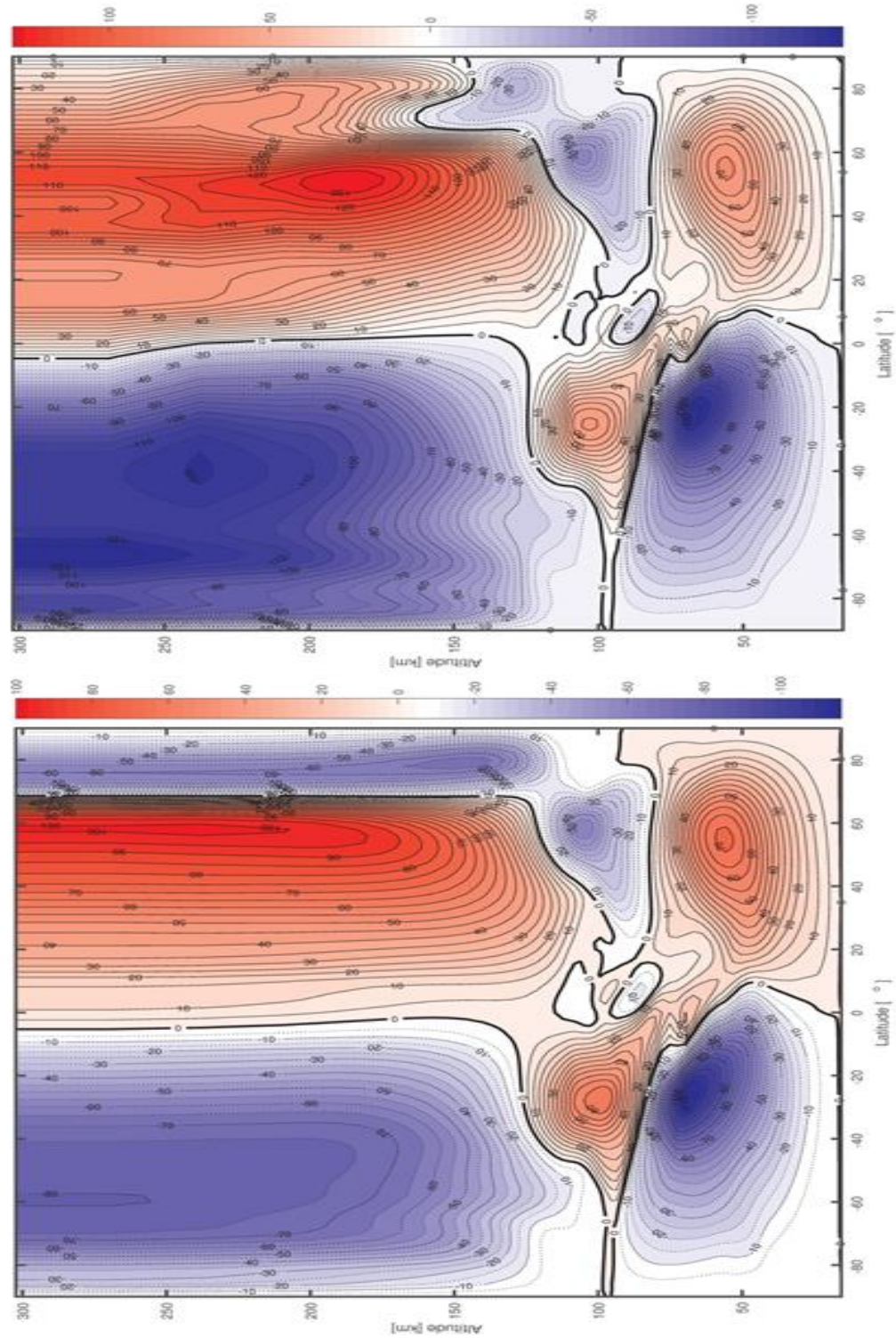
581 Figure 11 shows two versions of the CMAT2 zonally averaged zonal winds for 00 UT for December solstice
582 2008 (solar minimum conditions) from Hood (2019). These are latitude-height plots, where the height is from
583 15 km to 300 km. From about 250 km the contour lines become near vertical because the large molecular
584 viscosity of the upper thermosphere minimises the shear in the winds. The left hand plot is the standard run
585 using standard values of molecular viscosity. The right hand plot shows the contours for a simulation where the
586 molecular viscosity has been reduced by a factor of 100. The variation of the molecular viscosity with respect to
587 temperature (and consequently height for our purposes) has been tested theoretically and experimentally by
588 Dalgarno and Smith (1962), and the factor of 100 is an unrealistic extreme used to test the model. The
589 consequence is that the height at which contours become vertical is raised to closer to 280 km. This is a small
590 difference and certainly does not account for the apparent vertical gradient indicated by the difference between
591 the CHAMP and FPI zonal winds.

592 To end this section on the molecular viscosity of the upper thermosphere, two papers are referenced that report
593 observations and suggest other possible mechanisms to support winds varying with height. Recently Vadas and
594 Crowley (2017) published results from observations of 10 Travelling Ionospheric Disturbances at ~283 km
595 altitude, observed in 2007 with the TIDDBIT ionospheric sounder near Wallops Island, USA. They used ray
596 tracing on the TIDs and simultaneously measured a peak in the neutral wind at ~325 km altitude using a
597 sounding rocket. They found a serious discrepancy between where the gravity waves were predicted to dump
598 energy using conventional dissipative theory, and the observations from TIDDBIT and the rocket. Conventional
599 theory predicted that all the gravity waves should have dispersed at a scale height below the rocket
600 measurement. Consequently they have challenged convention and proposed that the molecular viscosity should
601 not increase as rapidly with altitude above 220 km. This may account for some of the difference between the
602 CHAMP and FPI zonal winds, but will need to be tested in future modelling studies.

603 The second paper by Song et al. (2009) states that the fastest acceleration of the neutrals occurs near 350 km in
604 the F layer, where the effective neutral-ion collision frequency maximizes (see their Figs. 6 and 7). Considering
605 the dynamic character of frequent changes of the IMF and the magnetospheric convection, the stronger
606 accelerations at F2 layer heights could result in temporary vertical neutral wind gradients. However, the 1-D
607 model approach neglects forces due to neutral pressure and effective molecular viscosity in the 3-D continuum
608 of the upper thermosphere. To describe correctly the long-range coupling on time scales from longer than few
609 seconds to less than 30 min, the inductive effect (Faraday's law) as well as the dynamic effect of the neutrals,
610 (in particular acceleration terms), need to be considered (Song and Vasyliunas, 2013).

611

612

613 **6.2 FPI Doppler shift to wind speed procedure**

614 Hypothesis B is that the FPI and/or CHAMP observations may need to be re-scaled. To start with the FPIs we
615 will look at the calculation of the Doppler shift and then at the height integration procedure of a ground-based
616 FPI.

617   The calculation of the wind speed requires few assumptions, though the process of fitting the FPI fringes is more

618   complicated (e.g. Makela et al., 2011). The wind speed u is determined from the Doppler shift of the wavelength

619    $\Delta\lambda$ of the moving volume of gas which emits at wavelength λ, where the free-space wavelength is λ_o and the

620   speed of light c (Eq. 3).

621
$$\lambda = \lambda_o \left(1 + \frac{u}{c}\right) = \lambda_o + \Delta\lambda \tag{3}$$

622   The speed of the volume of gas u is given by Eq. (4), which is proportional to the ratio of the Doppler shift in

623   fringe peak position (in bins) Δx; and the free spectral range (FSR), Δx_{FSR}. The FSR is the equivalent wavelength

624   shift to re-position a fringe from overlapping one order of the baseline wavelength λ_o, to the next order. The

625   other terms in Eq. (4) are the refractive index μ of the medium between the etalon plates and the separation of

626   the plates, d (Hecht and Zajak, 1980).

627
$$u = \left(\frac{\Delta x}{\Delta x_{FSR}}\right)\left(\frac{c\lambda_o}{2\mu d}\right) \tag{4}$$

628   The etalon gap is evacuated so $\mu=1$, and the other parameters are known. Thus for example, for an etalon gap d

629   = 10 mm, emission λ_o = 630 nm, free spectral range Δx_{FSR} = 150 bins, a Doppler shift of 1 bin (Δx = 1 bin)

630   would represent a wind of 63 ms^{-1}.

631   All the parameters for the scaling of the FPI winds in this equation are known. There is the issue of determining

632   the zero Doppler shift baseline because there is no laboratory source of the excited atomic oxygen. However, the

633   method used to determine the baseline (i.e., using a helium-neon source with the assumption that the vertical

634   component of the wind is negligible) introduces an average systematic offset error of at most 10-20 ms^{-1}, which

635   is small compared with horizontal wind magnitudes (Aruliah and Rees, 1995).

636

637   **Fig 12 left: height profile of CMAT2 zonal winds at Svalbard. Right: height profile of the red line emission intensity**
638   **profile from the Vlasov et al (2005) model.**
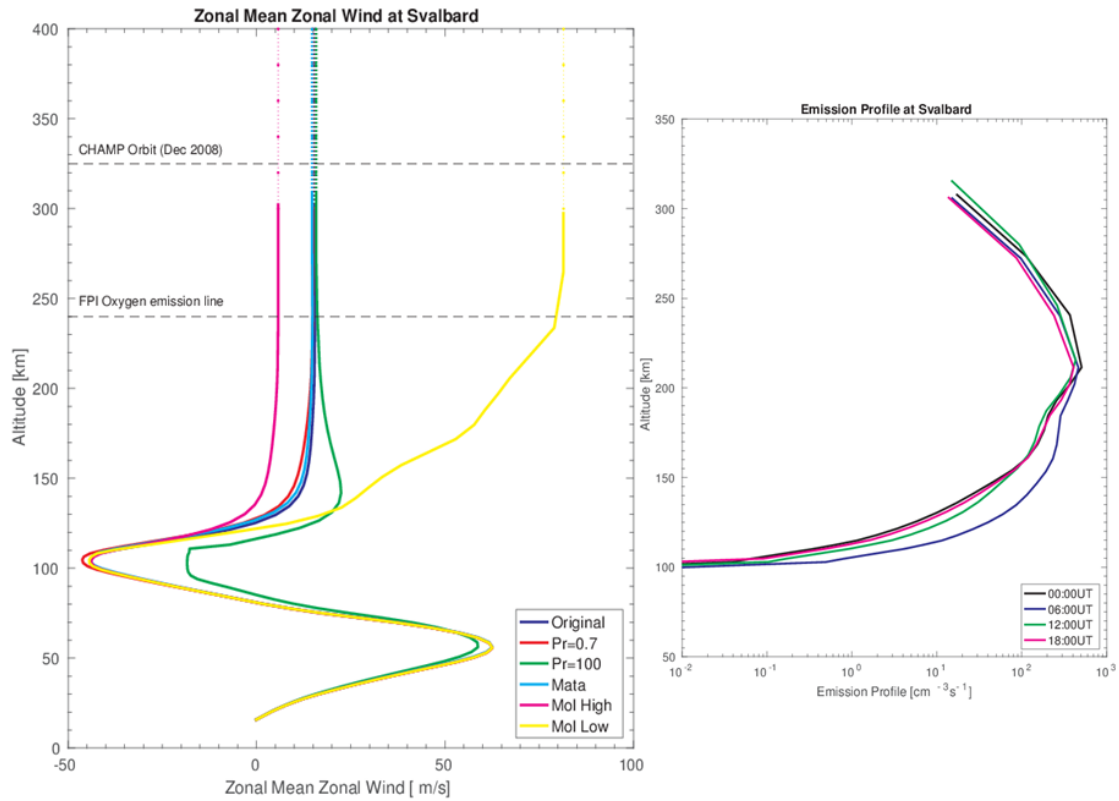
639   Figure 12 illustrates how ground-based FPIs make measurements of the neutral winds at 240 km altitude. The
640   left plot shows a height profile of the CMAT2 zonal mean zonal winds at the latitude of Longyearbyen. There
641   are 6 simulations to demonstrate the effect on the height profile of the zonal mean zonal winds when changing
642   the viscosity. CMAT2 uses a viscosity term that is the weighted mean divided by the scale height of two
643   coefficients of viscosity: the molecular viscosity μ_m; and the turbulent viscosity μ_t. The simulations represent a
644   comparison with the original molecular viscosity (dark blue). The other lines are for low (yellow - divided by
645   100) and high molecular viscosities (pink - doubled). The low and high turbulent viscosities are represented by
646   the Prandtl numbers 0.7 (red) and 100 (green), where 2 is the default value used in CMAT2. The Prandtl number
647   is related to the height at which gravity waves deposit momentum (Liu et al., 2013) and so may have relevance
648   for the Vadas and Crowley experiment (2017). The light blue line labelled "Mata" is an intermediate profile. As
649   can be seen, the molecular viscosity dominates in the thermosphere above 100 km and at the altitudes where the
650   FPI is measuring. The dark blue and yellow lines are representative of a vertical slice of Figure 11 left and right,
651   respectively, for the latitude of Longyearbyen.

652   The right hand plot of Figure 12 is a CMAT2 height profile of the 630 nm (red) line emission intensity based on
653   the Vlasov et al. (2005) model at 00UT, 06UT, 12UT and 18UT. The red line emission at night is dominated by
654   dissociative recombination of molecular oxygen ($O_2^+ + e \rightarrow O^* + O$). The altitude distribution of the 630 nm
655   emission has a peak emission altitude of between 220-250 km. However, the emission profile also has a full

656 width at half maximum intensity of around 50-70 km, i.e. sampling altitudes tens of km below and above the
657 emission peak. The ground-based FPI observes a height-integration of the emission along the line-of-sight. The
658 measured Doppler shift is therefore an integration of the Doppler shifts at all altitudes, weighted by the emission
659 profile. However, there are several reasons to justify why we are confident that the FPI provides a good sample
660 of the winds at ~240 km altitude. The excited atomic oxygen state in the O (^{1}D-^{3}P) transition is a forbidden
661 transition with a long life-time of ~110 sec (Bauer, 1973), which allows the excited atoms to thermalise before
662 emission and be representative of the surrounding gas. Below 200 km the molecular composition increases
663 significantly, and the long lifetime means that the 630 nm emission is quenched due to molecular collisions with
664 N_2 and O_2. Consequently we can assume there is minimal contribution of Doppler shifts from below 200 km
665 altitude, which is a region where the neutral wind magnitude has a large height dependence (note that the
666 emission intensity x-axis is a log scale; and that the horizontal winds at 100 km altitude are a few tens of ms^{-1}
667 while at 250 km altitude are a few hundreds of ms^{-1}). Above the altitude of the emission peak the flux falls off
668 rapidly with altitude, and also with distance from the FPI, which minimises the contribution of winds from the
669 region above. In addition, above 250 km the wind magnitudes begin to reach an asymptote. It therefore would
670 be expected that the satellites and ground-based FPIs should see very similar speeds and phases. With respect to
671 the FPI measured winds, the contribution of winds below the peak emission height may result in a small
672 underestimate of the winds at ~240 km altitude, which is investigated later in this section by modelling.

673 The tristatic FPI experiments by Aruliah et al (2005) and bistatic experiments by Anderson et al (2012)
674 indicated that the winds, neutral temperatures and 630 nm intensities were closely matched if the geometry
675 assumed an emission altitude of around 240 km. However, during auroral activity, when there is E-region
676 precipitation, the red line emission altitude can be lower, perhaps as low as 200 km. This means that the FPI
677 samples lower altitudes. Recently Gillies et al. (2017) used all-sky imagers to triangulate the peak emission
678 height of the 630 nm emission. They found that discrete auroral arcs showed a characteristic height of 200km.
679 The effect of particle precipitation in lowering the emission height was earlier noted by Sica et al. (1986). They
680 illustrated how decreased thermospheric temperatures measured by a Fabry-Perot spectrometer at College,
681 Alaska, were consistent with lower MSIS temperatures (Hedin et al., 1977) when weighted by a modelled
682 emission height profile. However, aurorae are limited to high latitudes and occur infrequently as illustrated by
683 Figure 13, which shows the frequency distributions of Kp values for the years (top) 2001-2003 representing
684 solar maximum; and (bottom) 2000-2009, i.e., for most of the period of the CHAMP lifetime. Aurora generally
685 occur during active periods when Kp > 4-5. Thus emission heights of 200 km are the exception rather than the
686 rule, and affect the average only minimally.

 Fig 13 Frequency distribution of Kp values. Top: 2001-2003 representing solar maximum. Bottom: 2000-2009

688 covering most of the period of the CHAMP lifetime.
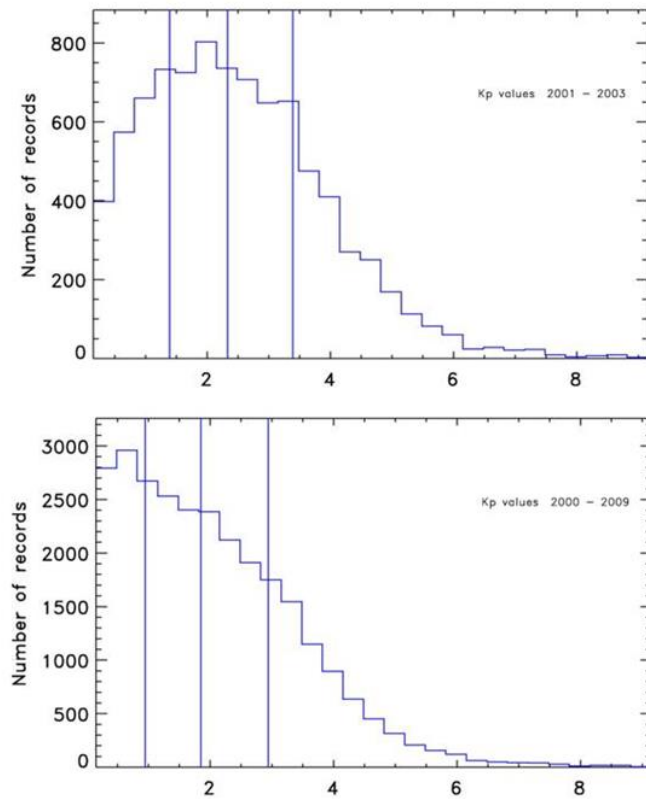
689 Fig 14 top: CMAT2 zonally averaged zonal winds for a quiet day on 1st December 2007 at Longyearbyen (left) and

690 Kiruna (right) for the winds at 180, 200 and 240km for comparison with the height integrated winds weighted using

691 an emission intensity profile from the Vlasov et al (2005) model. Bottom: the same for active conditions on 20th March

692 2015.

693
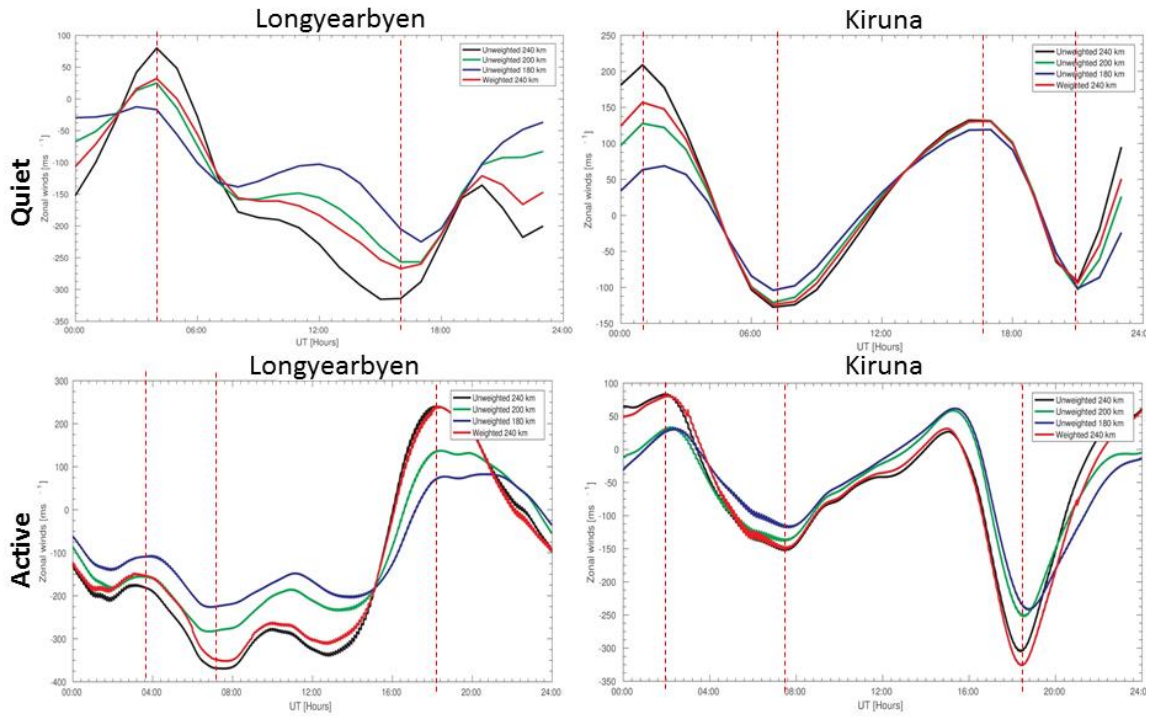
694 In order to assess by how much the FPI height integration method is underestimating winds, CMAT2 winds at

695 240 km are compared to a column integration average of CMAT2 winds weighted by the emission intensity

696 profile. Here the Vlasov et al (2005) model is applied with constants provided by Yiu (2014), and with CMAT2

697 winds interpolated to 10 km intervals for the integration. Figure 14 compares the CMAT2 zonally averaged

698 zonal winds at three heights: 180 (blue), 200 (green) and 240 km (black) with height integrated winds (red) for a

699 quiet day run on the 1st December 2007 (top panels) and an active day run on the 20th March 2015 (bottom

700 panels) for both Longyearbyen (left column) and Kiruna (right column). Figure 15 outlines the CMAT2 model

701 global view of the unweighted and weighted winds at 240km for 00, 06, 12 and 18UT.

702

703 **Fig 15: CMAT2 global zonal winds for a quiet day on 1st December 2007 for the winds at 240km and the height**
704 **integrated winds weighted using an emission profile from Vlasov et al (2005) model. From top left: 0UT, 6UT. From**
705 **bottom left: 12UT, 18UT.**

706
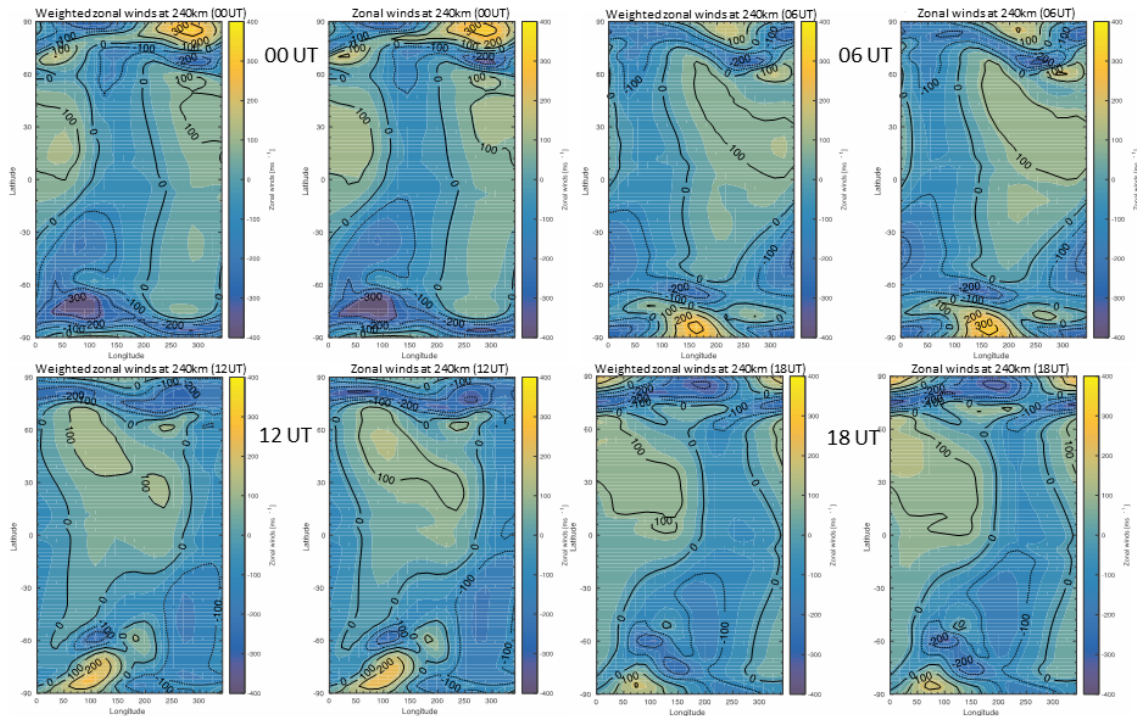
707 Figure 14 indicates that there are some significant differences between zonally averaged zonal winds with or
708 without height integration. The lower the altitude, the smaller the wind magnitude. There is also a slight change
709 in phase (to aid the eye these are indicated by vertical dashed lines placed at turning points for the weighted
710 winds). This is due to the increased collision frequency at lower altitudes due to greater density, and the
711 consequent shift in balance between pressure gradient and ion drag. When we look at the averaged diurnal
712 variation of the CHAMP and FPI winds, their phases are almost exactly the same. This would not be the case if
713 the FPI was observing winds dominated by Doppler shifts at 190 km altitude, where the phase would be
714 significantly different because the pressure gradient increases its dominance at lower altitudes. Comparing the
715 CMAT2 December 2007 model zonally averaged zonal winds at 240 km with the height integrated winds, the
716 most significant difference is for Longyearbyen during quiet conditions, which on calculating overall mean
717 values produces a 19% difference, that during active conditions reduces to a difference of 12%. The reverse
718 seems the case for Kiruna as the mean percentage difference increases from 3% to 14% between the quiet and
719 active days respectively. Note that the wind speed scales are different for each panel. For each time-series there
720 is no simple systematic trend. Figure 15 demonstrates these dissimilarities on a global scale; here the zonal
721 winds appear to be slightly more westward, as the eastward winds are diminished and the westward winds
722 enhanced. However, this is not the case for all times of day shown here, and does not visibly affect the wind
723 distributions to any large extent.

724

6.3 CHAMP cross track wind procedure

Satellites have provided global coverage of accelerometer measurements since 2001, in particular, the CHAMP satellite (e.g. Schlegel et al., 2005) and GRACE satellites (e.g. Tapley et al., 2004). These measurements of satellite drag have been converted to measurements of thermospheric mass density (e.g. Liu et al., 2005) and cross-track thermospheric wind measurements (e.g. Sutton et al, 2007, Liu et al., 2006, Förster et al., 2008). Thermospheric mass density was primarily estimated using Eq. 5 where $\underline{a}$ is the satellite acceleration, ρ the neutral mass density of the air, C_d refers to a dimensionless drag coefficient, using a constant frontal area A_{ref} of the satellite with mass m, and total velocity V relative to the atmosphere in the ram direction given by the unit vector $\hat{\underline{v}}$. This equation has been used for a first simple cross-track wind estimation, where the area and wind component were replaced by the horizontal side view and neutral wind direction perpendicular to the bulk flow, respectively.

$$\underline{a} = -\frac{1}{2}\rho\frac{C_d}{m}A_{ref}V^2\hat{\underline{v}} \tag{5}$$

For the first analysis, Liu et al. (2005) explained that they used a fixed drag coefficient value of $C_d = 2.2$. This is a de-facto standard value used for compact satellite orbit computations since the 1960s (e.g. Cook, 1965). This value was adopted by Jacchia when constructing his thermosphere density model, based on physical drag modelling of spherical satellites (Jacchia and Slowey, 1972). The drag coefficient is acknowledged to be very difficult to quantify, as is discussed extensively by, for example, Moe et al. (1995). The importance of the value of C_d is acknowledged by Liu et al (2006) and others who use the data, since it affects the scaling of the density and wind calculations. However, their interest was in the relative density and wind structures, rather than absolute values.

Since then the analysis has been refined considerably by taking into account lift, sideways, as well as drag forces on the satellite, resulting in smaller wind magnitudes as described by Doornbos et al. (2010). The GOCE satellite winds are closer in magnitude to ground-based FPI measurements (Dhadly et al., 2017), though still systematically larger in magnitude, where the difference has been found to increase with latitude. The systematic residual line-of-sight GOCE wind varied between 20 ms^{-1} at 50° MLAT to a maximum 150 ms^{-1} at 85° MLAT (see Figure 2 from Dhadly et al., 2018).

Another consideration is that CHAMP measures the cross-track wind component (Figures 1-2 and 3-4) which deviates from the pure zonal direction as measured by the FPIs (Figures 6 and 7). The geometry can be critical, in particular for the high-latitude Longyearbyen FPI, because the cross-track deviates from the zonal direction by about 13.3° in each direction respectively for the ascending and descending orbits. The meridional wind component at these high latitudes is much larger than the zonal one, so that the larger CHAMP measurements at this FPI could also (at least partially) be due to an "admixture" of the meridional wind component and the zonal wind. This has been discussed in section 5.1 to account for the difference between the average zonal winds measured during the ascending and descending orbits. To deal with this the UCL FPI zonal winds observed to the East and West are projected onto the CHAMP ascending and descending cross-track directions, and then averaged into 1-hour bins, thus replicating the CHAMP zonal wind averages (see Figures 7 and 8). Despite this

761 re-calculation there is a wide range of values of the CHAMP/FPI ratios (see Figure 10a, b), which reinforces the

762 message that the satellite aerodynamic coefficients are difficult to determine absolutely, which is in addition to

763 some systematic factor between the CHAMP and FPI measurements. This difficulty is well known in the

764 satellite engineering community, but perhaps less so in the aeronomy community.

765

6.4 Comparison with EISCAT radar ion velocities

767 Finally, a very important consideration is how the average winds compare with ion velocities. At high latitudes

768 the ion velocities are generally larger than the neutral winds owing to the $\underline{E}$ x $\underline{B}$ drift driven by the

769 magnetospheric electric field. Davies et al (1995) provided a statistical analysis of E- and F- region ion

770 velocities observed on 20 March 1996 in order to compare measurements by the EISCAT incoherent scatter

771 radars and the CUTLASS coherent scatter radar. The scatter plot of ion velocities from this study (their Figure

772 5) indicated a cluster of values in the range of a few hundred ms^{-1}, with only a small fraction of measurements

773 greater than 500 ms^{-1}.

774 Fiori et al (2016) compared ion velocities measured by the Electric Field Instrument on Swarm with the CS10

775 statistical ionospheric convection model by Cousins and Shepherd (2010) which is based on 8 years of data

776 (1998-2005) collected by 16 SuperDARN coherent scatter radars. The climatology represented by the CS10

777 model in Fiori et al's Figure 3a indicates speeds in the few hundreds of ms^{-1}, while the instantaneous values

778 along the Swarm satellite pass (their Figure 3d) show much stronger drift peak values on the resolution level of

779 seconds or shorter. Even after allowing for offsets, their 1-sec resolution corrected cross-track ion drifts achieve

780 horizontal velocities well over 1,000 ms^{-1}, which probably indicates the highly dynamic behaviour in the auroral

781 regions compared with quasi-stable conditions used for empirical models. However, recently Koustov et al.

782 (2019) compared the Swarm cross-track ion drifts with the SuperDARN radar network and found that the

783 Swarm ion velocities are a factor of 1.5 larger. They suggest reasons for the disparity, including refining the

784 calibration of Swarm and the differences in spatial/temporal resolution.

785 Aruliah et al. (1996) presented the seasonal and solar cycle variation of hourly averaged ion velocities from 300

786 days of EISCAT Tromsø UHF radar measurements between 1984-1990. The tristatic EISCAT radar

787 observations for an altitude of 275 km were collected from Common Programmes 1, 2 and 3, at time resolutions

788 of 2-3 mins, with full 24 hours coverage. The hourly averaged ion velocities for December solstice periods were

789 up to 100-200 ms^{-1}, and the largest average ion velocities were around 300 ms^{-1} during the March equinox

790 period at solar maximum. Aruliah et al. (2005) later reported observations of a common volume using a

791 configuration of tristatic FPI observations of the thermospheric winds and temperatures co-located with tristatic

792 EISCAT radar measurements of ionospheric parameters at 250 km altitude. The observations showed that the

793 neutral winds were on average around 50% of the magnitude of the ion velocities when averaged over 15 min.

794 Griffin et al. (2004) determined seasonal and solar cycle climatologies of meridional winds at Kiruna using FPI

795 Doppler shifts, and derived from field-aligned ion velocities (Salah and Holt, 1974), which were compared with

796 physical (CTIM, Fuller-Rowell et al., 1988) and empirical models (HWM, Hedin et al, 1988; MWM, Miller et

797 al., 1997). The climatologies all showed meridional winds up to ~250 ms^{-1}. Although this method does not give

the zonal wind magnitude, it gives some indication of typical magnitudes owing to the diurnal variation of winds seen by a single site as the Earth rotates.

Förster et al. (2008) presented a statistical comparison of observed averaged neutral wind velocities within the polar cap (magnetic latitudes > 80°) for the year 2003 showing the dependence on the IMF orientation based on statistical analyses of CHAMP accelerometer data with average ion drift estimates for the same time interval and IMF conditions based on EDI Cluster measurements. These comparisons were done for both the Northern and the Southern Hemisphere separately in their Tables 1 and 2, respectively. Depending on the IMF clock angle orientation, the ratio between average neutral wind magnitudes and average ion drift speeds varies between about 60% and around 100%. Interestingly, there is a characteristic interhemispheric difference with respect to the IMF orientation and slightly larger ion drift velocities on average in the Northern Hemisphere (cf. Förster and Cnossen, 2013; Förster et al., 2017), but the overall average amounts to a ratio of about 0.90 to 0.95 for, note well, within the polar cap region > 80° magnetic only. The FPI in Longyearbyen at 75.4° N (see Table 2) comes closest to this region. Ion drag is the dominating forcing term here for the neutral gas, while near the auroral oval, where the KEOPS FPI station in Kiruna at 65.1° N is located, the balance between the different forces, in particular pressure gradient terms, Coriolis and centrifugal forces, and ion drag, play a role. There the ratio between the average neutral wind and ion drag magnitudes is certainly smaller, corresponding to the EISCAT observations cited above.

7 Conclusions

A comparison is presented here of thermospheric zonal winds during winter months between 2001-2007 measured by the CHAMP satellite in the altitude region 350-400 km, and by ground-based FPIs, at Kiruna and Longyearbyen, measured at about 240 km altitude. The satellite accelerometer measurements of drag are used to derive cross-track winds, while the FPIs use the Doppler shift of the 630 nm emission. The satellite measurements are collected for a region within 2° latitude of the FPI sites, which is within the field of view of the FPI East and West look directions. The phases of the winds agree very well, but the CHAMP average zonal winds are a factor 1.5-2.0 larger than the FPI average zonal winds. The factor is not simple. In particular there is a difference in the factor for the auroral site and the polar cap site, so it appears that the factor is dependent on location, possibly latitude. The factor also appears to have an irregular time dependence.

The UCL Longyearbyen FPI winds are consistent with FPI measurements made 20 years previously by the University of Alaska using a different FPI and detector (photometer in 1980, EMCCD in 2001). Earlier studies of average ion velocities from the EISCAT Tromsø UHF radar compared with the UCL FPI at KEOPS indicate that in the auroral zone the average ion velocities are about twice the average neutral wind speeds (Aruliah et al., 1996 and 2005). However, the CHAMP average zonal winds at KEOPS presented here have magnitudes similar to the average *ion* velocities of the December solstice values presented by Aruliah et al (1996). This is probably the key argument indicating that the CHAMP magnitudes are too large. It is important to determine the absolute wind values correctly since the difference between the ion flow and neutral wind vectors determine the acceleration of the neutral gas, and the amount of Joule heating of the thermosphere.

Satellites play a crucial role in upper atmosphere research by filling in the extensive gaps between ground-based observations. But for satellite drag measurements, we note that satellite aerodynamic coefficients are difficult to determine absolutely. Satellites provide 3-dimensional coverage at high spatial resolution, in addition to high temporal resolution. Meanwhile, ground-based instruments are sparse, land-based, and not always operational on a 24/7 basis owing to operational costs (e.g. incoherent scatter radars) or observing constraints (e.g. only night-time and clear sky observations for optical instruments). Having uncovered this discrepancy between ground-based FPI optical measurements and satellite drag measurements of winter winds, it is imperative to determine if it is a real altitude dependence, or if some re-scaling of winds, is necessary for winds determined from either, or both, of FPI height-integrated Doppler shifts or satellite drag measurements. Both possibilities will affect our current modelling of the upper atmosphere. We may also need to rethink the procedure of comparing different spatial and temporal resolutions of in-situ satellite versus remote ground-based FPI measurements at high latitudes.

Author contributions. This paper is the result of many years of collaboration between AA and MF after noticing the significant difference between FPI and CHAMP winds. AA provided the FPI data, MF provided the CHAMP data. RH provided the model simulations, IM provided technical support for the FPIs, and ED provided expertise on converting accelerometer data to winds.

Competing interests. The authors declare that they have no conflict of interest.

Data availability. The CHAMP accelerometer neutral wind observations used in this study are available at http://doi.org/10.5880/GFZ.1.1.2019.001 (Förster and Doornbos, 2019).

Acknowledgements. We thank the staff at the Kjell Henriksen Observatory and ESRANGE for hosting the FPIs and their generous on-site assistance. Support for the FPI operations have come from the European Office of Aerospace Research and Development (grant FA9550-17-1-0019). There has been NERC support of ALA (grants NE/P001556/1 and NE/N004051/1). The CHAMP mission is sponsored by the Space Agency of the German Aerospace Center (DLR) through funds of the Federal Ministry of Economics and Technology, following a decision of the German Federal Parliament (grant code 50EE0944). The data retrieval and operation of the CHAMP satellite by the German Space Operations Center (GSOC) of DLR is acknowledged. EISCAT is an international association supported by research organisations in China (CRIRP), Finland (SA), France (CNRS, till end 2006), Germany (DFG), Japan (NIPR and STEL), Norway (NFR), Sweden (VR), and the United Kingdom (STFC). We also acknowledge support from the International Space Science Institute for sponsoring meetings of the international team #308 on 'M-I-T Coupling: Differences and similarities between the two hemispheres', which helped this collaboration (http://www.issibern.ch/teams/twohemispheres/).

873

874 **References:**

875 Anderson, C., Conde, M., and McHarg, M. G.: Neutral thermospheric dynamics observed with two scanning
876   Doppler imagers: 1. Monostatic and bistatic winds, J. Geophys. Res.,117, A03304,
877   doi:10.1029/2011JA017041, 2012.

878 Aruliah A.L., Rees, D.: The Trouble with Thermospheric Vertical Winds: Geomagnetic, Seasonal and Solar
879   Cycle Dependence at High Latitudes, J. Atmos. Terr. Phys., 57, 597-609, 1995

880 Aruliah A.L., Farmer, A. D., Rees, D., Brändström, U.: The Seasonal Behaviour of High-Latitude
881   Thermospheric Winds and Ion Velocities Observed Over One Solar Cycle, J. Geophys. Res., 101, 15701-
882   15711, 1996

883 Aruliah, A. L. and Griffin, E. M.: Evidence of meso-scale structure in the high-latitude thermosphere, Ann.
884   Geophys., 37–46, 2001.

885 Aruliah, A. L., Griffin, E. M., Aylward, A. D., Ford, E. A. K., Kosch, M. J., Davis, C. J., Howells, V. S. C.,
886   Pryce, E., Middleton, H., Jussila, J.: First direct evidence of meso-scale variability on ion-neutral dynamics
887   using co-located tristatic FPIs and EISCAT radar in Northern Scandinavia, EISCAT workshop special issue
888   Annales Geophys., 23, 147-162, 2005

889 Bauer, S.J.: Physics and chemistry in space, Vol 6 of Physics of planetary ionospheres, Springer-Verlag, 1973

890 Bruinsma, S. L., Doornbos, E., Bowman, B.R.: Validation of GOCE densities and evaluation of thermosphere
891   models Advances in Space Research, Volume 54, Issue 4, 576-585.10.1016/j.asr.2014.04.008, 2014.

892 Cook, G.E.: Satellite drag coefficients, Planet. Space Sci., 13, 929, 1965

893 Cousins, E. D. P., and S. G. Shepherd (2010), A dynamical model of high‐latitude convection derived from
894   SuperDARN plasma drift measurements, J. Geophys. Res., 115, A12329, doi:10.1029/2010JA016017.

895 Dalgarno, A., and Smith, F. J.: The thermal conductivity and viscosity of atomic oxygen, Planet.Space.Sci., 9, 1-
896   2, 1962.

897 Davies, J.A., Lester, M., Milan, S.E., Yeoman, T. K.: A comparison of velocity measurements from the
898   CUTLASS Finland radar and the EISCAT UHF system, Ann.Geophys., 17, 892-902, 1999.

899 Deehr, C. S., Sivjee, G. G., Egeland, A., Henriksen, K., Sandholt, P. E., Smith, R., Sweeney, P., Duncan, C.,
900   Gilmer, J.: Ground-based observations of F region aurora associated with the magnetospheric cusp, J.
901   GEOPHYS. RES., 85, 2185-2192, 10.1029/JA085iA05p02185, 1980.

902 Dhadly, M., Emmert, J., Drob, D., Conde, M., Doornbos, E., Shepherd, G., Makela, J., Wu, Q., Niciejewski, R.,
903   and Ridley, A.: Seasonal dependence of northern high-latitude upper thermospheric winds: A quiet time
904   climatological study based on ground-based and space-based measurements, Journal of Geophysical
905   Research (Space Physics), 122, 2619-2644, 10.1002/2016JA023688, 2017

906 Dhadly, M., Emmert, J., Drob, D., Conde, M., Shepherd, G., Makela, J., Wu, Q., Niciejewski, R., and Ridley,
907   A.: Seasonal Dependence of geomagnetic active-time northern high-latitude upper thermospheric winds, J.
908   GEOPHYS. RES., 123, 739-754, https://doi.org/10.1002/2017JA024715, 2018

909 Doornbos, E, Ijssel, J., Lühr, H., Förster, M., and Koppenwallner, G:. Neutral density and crosswind
910   determination from arbitrarily oriented multiaxis accelerometers on satellites. Journal of Spacecraft and
911   Rockets, 47(4): 580–589, 2010. doi:10.2514/1.48114, 2010

Drob, D. P., Emmert, J. T., Meriwether, J. W., Makela, J. J., Doornbos, E, Conde, M., Hernandez, G., Noto, J., Zawdie, K. A., McDonald, S. E., Huba, J. D., and Klenzing, J. H.: An update to the Horizontal Wind Model (HWM): The quiet time thermosphere, Earth and Space Science, 2, 301-319, 10.1002/2014EA000089, https://doi.org/10.1002/2014EA000089,2015

Emmert, J.T., Hernandez, G., Jarvis, M. J., Niciejewski, R. J., Sipler, D. P., and Vennerstrom, S.: Climatologies of nighttime upper thermospheric winds measured by ground-based Fabry-Perot interferometers during geomagnetically quiet conditions: 2. High-latitude circulation and interplanetary magnetic field dependence, J. Geophys. Res., 111, A12303, doi:10.1029/2006JA011949, 2006b.

Fiori, R. A. D., Koustov, A. V., Boteler, D. H., Knudsen, D. J., & Burchill, J. K.: Calibration and assessment of Swarm ion drift measurements using a comparison with a statistical convection model. Earth, Planets and Space, 68(1), 100. http://doi.org/10.1186/s40623-016-0472-7, 2016.

Forbes, J. M., Roble, R. G., and Marcos, F. A.: Magnetic activity dependence of high−latitude thermospheric winds and densities below 200 km, J. Geophys. Res., 98, 13,693–13,702, 1993.

Ford, E.A.K., Aruliah, A.L., Griffin, E.M., McWhirter, I.: High time resolution measurements of the thermosphere from Fabry-Perot Interferometer measurements of atomic oxygen, Annales Geophys., 25, 1269 – 1278, 2007.

Förster, M., Rentz, S., Köhler, W., Liu, H., and Haaland, S. E.: IMF dependence of high-latitude thermospheric wind pattern derived from CHAMP cross-track measurements, Ann. Geophys., 26, 1581–1595, 2008.

Förster, M., Haaland, S.E., and Doornbos, E., Thermospheric vorticity at high geomagnetic latitudes from CHAMP data and its IMF dependence, Ann. Geophys., 29, 181-186, doi:10.5194/angeo-29-181-2011, 2011.

Förster, M., and Cnossen, I.: Upper atmosphere differences between northern and southern high latitudes: The role of magnetic field asymmetry, J. Geophys. Res. Space Physics, *118*, 5951–5966, doi:10.1002/J.Geophys.Res.a.50554, 2013.

Förster, M., Doornbos, E., and Haaland S.: The role of the upper atmosphere for dawn-dusk differences in the coupled magnetosphere-ionosphere-thermosphere system", in: Dawn-Dusk Asymmetries in Planetary Plasma Environments, eds. Stein Haaland, Andrei Runov and Colin Forsyth, John Wiley Publications, AGU Geophysical Monograph, Vol. 230, 125-142, ISBN: 978-1-119-21632-2, 2017.

Förster, Matthias; Doornbos, Eelco (2019): Upper thermosphere neutral wind cross-track component deduced from CHAMP accelerometer data. GFZ German Research Centre for Geosciences. http://doi.org/10.5880/GFZ.1.1.2019.001

Foster, J. C., Holt, J. M., Musgrove, R. G., and Evans, D. S.: Ionospheric convection associated with discrete levels of particle precipitation, Geophys. Res. Lett., 13, 656, 1986.

Fuller-Rowell, T. J.: Modelling the solar cycle change in nitric oxide in the thermosphere and upper mesosphere, J. Geophys. Res., 98, 1571, 1992.

Fuller-Rowell, T.J., Rees, D.: Interpretation of an Anticipated Long-Lived Vortex in the Lower Thermosphere Following Simulation of an Isolated Substorm, Planet. Space Sci., 32, 69-85, 1984

Fuller-Rowell T.J., Evans, D.S.: Height Integrated Pedersen and Hall Conductivity Patterns Inferred from the TIROS-NOAA Satellite Data, J. GEOPHYS. RES., 92, 7606-7618, 1987

950 Fuller-Rowell, T. J., Rees, D., Quegan, S., Moffett, R. J., Bailey, G.J.: Simulations of the seasonal and UT
951   variations of the thermosphere and ionosphere using a coupled, three-dimensional, global model, Pur. A.
952   Geoph., 127, 189–217, 1988.

953 Fuller-Rowell, T. J., Rees, D., Quegan, S., Moffett, R. J., Codrescu, M. V., and Millward, G. H.: A coupled
954   thermosphere ionosphere model, Solar terrestrial energy program (STEP), handbook of ionospheric models,
955   (Ed) Schunk, R. W., 1996.

956 Gillies, M. D., Knudsen, D., Donovan, E., Jackel, B., Gillies, R., Spanswick, E.: Identifying the 630 nm auroral
957   arc emission height: A comparison of the triangulation, FAC profile, and electron density methods, J.
958   Geophys. Res. Space Physics, 122, doi:10.1002/2016JA023758, 2017.

959 Griffin, E.M., Aruliah, A. L., Müller-Wodarg, I. C. F., Aylward, A. D.: Comparison of High-Latitude
960   Thermospheric Meridional Winds II: Combined FPI, Radar and Model Climatologies, Ann. Geophys, 22,
961   863-876, 2004.

962 Griffin, E. M., Müller-Wodarg, I. C. F., Aruliah, A., and Aylward, A.: Upper thermospheric neutral wind and
963   temperature measurements from an extended spatial field, Ann. Geophys., 26, 2649– 2655, 2008.

964 Harang, L.: The mean field of disturbance of polar geomagnetic storms, Terr. Mag. Atmos. Elec., 51, 353-380,
965   1946.

966 Harris, M.: A New Coupled Middle Atmosphere and Thermosphere General Circulation Model: Studies of
967   Dynamic, Energetic and Photochemical Coupling in the Middle and Upper Atmosphere. PhD Thesis,
968   University of London, 2001

969 Harris, M. J., Arnold, N. F., and Aylward, A. D.: A study into the effect of the diurnal tide on the structure of
970   the background mesosphere and thermosphere using the new coupled middle atmosphere and thermosphere
971   (CMAT) general circulation model, Ann. Geophys., 20, 225–235, doi:10.5194/angeo-20-225-2002, 2002.

972 Hecht, E., Zajac, A.: Optics, Addison-Wesley Publishing Company, 1980.

973 Hedin A. E., Salah, J. E., Evans, J. V., Reber, C. A., Newton, G. P., Spencer, N. W., Kayser, D. C., Alcayde, D.,
974   Bauer, P., Cogger, L., McClure, J. P.: A Global Thermospheric Model Based on Mass Spectrometer and
975   Incoherent Scatter Data MSIS 1. N_2 Density and Temperature, J.Geophys.Res., 82, 2139-2147, 1977.

976 Hedin A.E., Biondi, M. A., Burnside, R. G., Hernandez, G., Johnson, R. M., Killeen, T. L., Mazaudier, C.,
977   Meriwether, J. W., Salah, J. E., Sica, R. J., Smith, R. W., Spencer, N. W., Wickwar, V. B., Virdi, T. S.:
978   Revised Global Model of Thermospheric Winds Using Satellite and Ground-Based Observations, J.
979   Geophys. Res. Space Physics, 96, 7657-7688, 1991.

980 Hedin, A. E., et al. (1996), Empirical wind model for the upper, middle and lower atmosphere, J. Atmos. Terr.
981   Phys., 58, 1421–1447, doi:10.1016/0021-9169(95)00122-0.

982 Helleputte, T. V., Doornbos, E., and Visser, P.: CHAMP and GRACE accelerometer calibration by GPS-based
983   orbit   determination.   Advances   in   Space   Research,   43(12),   1890–1896.
984   http://doi.org/10.1016/j.asr.2009.02.017, 2009.

985 Hood, R. K. E., Effects of field-aligned currents in the ionosphere-thermosphere system, PhD Thesis, University
986   College London, UK, 2018

987 Jacchia, L. G., and Slowey, J. W.: A supplemental catalog of atmospheric densities from satellite-drag analysis
988   (No. 348). SAO Special Report, 1972.

989 Killeen, T. L., Smith, R. W., Hays, P. B., Spencer, N. W., Wharton, L. E., McCormac, F. G.: Neutral winds in
990   the high latitude winter F-region: Coordinated observations from ground and space, Geophys. Res. Lett., 11,
991   311-314, 1984.

992 Killeen T.L., Won, Y.-I., Niciejewski, R.J., Burns, A.G.: Upper Thermosphere Winds and Temperatures in the
993   Geomagnetic Polar Cap: Solar Cycle, Geomagnetic Activity and IMF Dependencies, J. Geophys. Res., 100,
994   21327-21342, 1995.

995 Koustov, A. V., Lavoie, D. B., Kouznetsov, A. F., Burchill, J. K.,Knudsen, D. J., & Fiori, R. A. D., A
996   comparison of cross-track ion drift measured by the Swarm satellites and plasma convection velocity
997   measured by SuperDARN. Journal of Geophysical Research: Space Physics, 124, 4710-4724.
998   https://doi.org/10.1029/2018JA026245, 2019.

999 Liu, H., Lühr, H., Henize, V., and Köhler, W.: Global distribution of the thermospheric total mass density
1000   derived from CHAMP, J. Geophys. Res., 110, A04301, doi:10.1029/2004JA010741, 2005.

1001 Liu, H., Lühr, H.,Watanabe, S., Köhler,W., Henize, V., and Visser, P.: Zonal winds in the equatorial upper
1002   thermosphere: Decomposing the solar flux, geomagnetic activity, and seasonal dependencies, J. Geophys.
1003   Res., 111, A07307, doi:10.1029/2005JA011415, 2006.

1004 Liu, H., Doornbos, E., & Nakashima, J.: Thermospheric wind observed by GOCE: Wind jets and seasonal
1005   variations. Journal of Geophysical Research: Space Physics, 121(7), 6901–6913.
1006   http://doi.org/10.1002/2016JA022938, 2016.

1007 Liu, X., Xu, J., Yue, J. & Vadas, S. L., Numerical modeling study of the momentum deposition of small
1008   amplitude gravity waves in the thermosphere, Annales Geophysicae, 31(1), 1-14, 2013

1009 Makela, J. J., Meriwether, J. W., Huang, Y., Sherwood, P. J.: Simulation and analysis of a multi-order imaging
1010   Fabry-Perot interferometer for the study of thermospheric winds and temperatures, Applied Optics, 50,
1011   4403-4416, 2011.

1012 March, G., Doornbos, E. N. and Visser, P. N. A. M.: High-fidelity geometry models for improving the
1013   consistency of CHAMP, GRACE, GOCE and Swarm thermospheric density data sets, Advances in Space
1014   Research, 63, 213-238, 10.1016/j.asr.2018.07.009, 2018.

1015 March, G., E. N. Doornbos, and P. N. A. M. Visser, High-fidelity geometry models for improving the
1016   consistency of CHAMP, GRACE, GOCE and Swarm thermospheric density data sets, Advances in Space
1017   Research, 63, 213-238, 10.1016/j.asr.2018.07.009, 2019

1018 Marcos, F. A. and Forbes, J. M.: Thermospheric wind from the satellite electrostatic triaxial accelerometer
1019   system, J. Geophys. Res., 90, 6543–6552, 1985.

1020 McWhirter I., Rees, D., Greenaway, A. H.: Miniature Imaging Photon Detectors III.~An Assessment of the
1021   Performance of the Resistive Anode IPD, J. Phys. E.: Sci. Instrum., 15, 145-150, 1982.

1022 McWhirter, I., Electron Multiplying CCDs - New Technology for Low Light Level Imaging, Proceedings of
1023   33rd Annual European Meeting on Atmospheric Studies by Optical Methods, IRF Sci. Rep., 292, 61-66,
1024   2008.

1025 Mehta, P. M., Walker, A. C., Sutton, E., & Godinez, H. C.: New density estimates derived using accelerometers
1026   on-board the CHAMP and GRACE satellites. Space Weather, 15(4), 558–576.
1027   http://doi.org/10.1002/2016SW001562, 2017.

1028 Moe, Mildred. M., Wallace, Steven D., Moe, Kenneth : The upper mesosphere and lower thermosphere, A
1029   review of experiment and theory, Geophysical Monograph 87, 1995

1030 Quegan, S., Bailey, G. J., Moffett, R. J., Heelis, R. A., Fuller-Rowell, T. J., Rees, D., and Spiro, A. W.: A
1031   theoretical study of the distribution of ionisation in the high-latitude ionosphere and the plasmasphere: First
1032   results of the mid-latitude trough and the light ion trough, J. Atm. Terr. Phys., 44, 619, 1982.

1033 Rees, D., Fuller-Rowell, T. J., Gordon, R., Smith, M. F., Maynard, N. C., Heppner, J. P., Spencer, N. W.,
1034   Wharton, L., Hays, P. B., and Killeen, T. L.: A theoretical and empirical study of the response of the high
1035   latitude thermosphere to the sense of the "Y" component of the interplanetary magnetic field, Planet. Space
1036   Sci., 34, 1–40, 1986.

1037 Reigber, C., Lühr, H., and Schwintzer, P.: CHAMP mission status, Adv. Space Res., 30, 129–134, 2002.

1038 Roble, R. G., Ridley E. C., and Dickenson, R. E.: On the global mean structure of the thermosphere, J. Geophys.
1039   Res., 92, A8, 8745–8758, 1987.

1040 Ronksley, Amy, Optical remote sensing of mesoscale thermospheric dynamics above Svalbard and Kiruna, PhD
1041   thesis, UCL, London, UK., 2016.

1042 Salah, J. E. and Holt, J. M.: Midlatitude thermospheric winds from incoherent scatter radar and theory, Radio
1043   Sci., 9, 301–313, 1974.

1044 Schlegel, K., Lühr, H., St.-Maurice, J.-P., Crowley, G., and Hackert, C.: Thermospheric density structures over
1045   the polar regions observed with CHAMP, Annales Geophysicae, 23, 1659–1672, 2005.

1046 Shepherd, S. G.: Altitude-adjusted corrected geomagnetic coordinates: Definition and functional
1047   approximations, J. Geophys. Res. Space Physics, 119, doi:10.1002/2014JA020264, 2014.

1048 Sica R. J., Rees, M. H., Roble, R. G., Hernandez, G., Romick, G. J.: The Altitude Region Sampled by Ground-
1049   Based Doppler Temperature Measurements of the OI 15867K Emission Line in Aurorae, Planet. Space Sci.,
1050   34, 483-488, 1986.

1051 Song, P., Vasyliūnas, V. M., and Zhou, X.-Z.: Magnetosphere-ionosphere/thermosphere coupling: Self-
1052   consistent solutions for a one-dimensional stratified ionosphere in three-fluid theory, J. Geophys. Res., 114,
1053   A08213, doi:10.1029/2008JA013629, 2009.

1054 Song, P., and Vasyliūnas, V. M.: "Inductive-dynamic coupling of the ionosphere with the thermosphere and the
1055   magnetosphere", in: 'Modeling the Ionosphere-Thermosphere System', edited by J. Huba, R. Schunk, and G.
1056   Khazanov, American Geophysical Union, Washington DC,10.1029/2012GM001308, Geophysical
1057   Monograph Series 201, 201-215, 2013.

1058 Sutton, E. K., Nerem, R. S., & Forbes, J. M.: Density and Winds in the Thermosphere Deduced from
1059   Accelerometer Data. Journal of Spacecraft and Rockets, 44(6), 1210–1219. http://doi.org/10.2514/1.28641,
1060   2007.

1061 Tapley, B.D., Bettadpur, S., Watkins, M., and Reigber, C.: The gravity recovery and climate experiment:
1062   Mission overview and early results, Geophys. Res. Lett., 31, L09607, DOI: 10.1029/2004GL019920, 2004.

1063 Torr, M. R., Richards, P. G., and Torr, D. G.: A new determination of ultraviolet heating efficiency in the
1064   thermosphere, J. Geophys.Res., 85, 6819, 1980a.

1065 Torr, M. R., Richards, P. G., and Torr, D. G.: The solar ultraviolet heating efficiency in the mid-latitude
1066   thermosphere, Geophys.Res. Lett., 6, 673, 1980b.

1067   Vadas, S. L. and Crowley, G.: Neutral wind and density perturbations in the thermosphere created by gravity

1068   waves observed by the TIDDBIT sounder, J. Geophys. Res. Space Physics, *122*, 6652–6678,

1069   doi:10.1002/2016JA023828, 2017.

1070   Visser, T., March, G., Doornbos, E., de Visser, C., & Visser, P.: Horizontal and vertical thermospheric cross-

1071   wind from GOCE linear and angular accelerations. Advances in Space Research.

1072   http://doi.org/10.1016/j.asr.2019.01.030, 2019.

1073   Vlasov, M. N., Nicolls, M. J., Kelley, M. C., Smith, S. M., Aponte, N., and Gonzalez, S. A: Modeling of

1074   airglow and ionospheric parameters at Arecibo during quiet and disturbed periods in October 2002, J.

1075   Geophys. Res., 110, A07303, doi:10.1029/2005JA011074, 2005.

1076   Yiu, H.C.I: High latitude thermosphere meso-scale studies and long-term database investigations with the new

1077   Scanning Doppler Imager and Fabry-Perot Interferometers, Ph.D. Thesis, Univ. of London, London, UK,

1078   2014.